AFRL-RX-WP-TP-2009-4138

MICROSTRUCTURE-SENSITIVE MODELING OF HIGH CYCLE FATIGUE (PREPRINT)

Craig Przybyla, Rajesh Prasannavenkatesan, Nima Salajegheh, and David L. McDowell

Metals Branch
Metals, Ceramics and NDE Division

MARCH 2009

STINFO COPY

AIR FORCE RESEARCH LABORATORY
MATERIALS AND MANUFACTURING DIRECTORATE
WRIGHT-PATTERSON AIR FORCE BASE, OH 45433-7750
AIR FORCE MATERIEL COMMAND
UNITED STATES AIR FORCE

REPORT DOCUMENTATION PAGE

1. REPORT DATE *(DD-MM-YY)*	2. REPORT TYPE	3. DATES COVERED *(From - To)*
March 2009	Journal Article Preprint	01 March 2009 – 01 March 2009

4. TITLE AND SUBTITLE

MICROSTRUCTURE-SENSITIVE MODELING OF HIGH CYCLE FATIGUE (PREPRINT)

5a. CONTRACT NUMBER
In-house

5b. GRANT NUMBER

5c. PROGRAM ELEMENT NUMBER
62102F

6. AUTHOR(S)

Craig Przybyla (AFRL/RXLMN)

Rajesh Prasannavenkatesan, Nima Salajegheh, and David L. McDowell (Georgia Institute of Technology)

5d. PROJECT NUMBER
4347

5e. TASK NUMBER
RG

5f. WORK UNIT NUMBER
M02R3000

7. PERFORMING ORGANIZATION NAME(S) AND ADDRESS(ES)

Metals Branch (RXLMN)
Metals, Ceramics and NDE Division
Materials and Manufacturing Directorate
Wright-Patterson Air Force Base, OH 45433-7750
Air Force Materiel Command, United States Air Force

GWW School of Mechanical Engineering and School of Materials Science & Engineering
Georgia Institute of Technology
Atlanta, GA 30332-0405

8. PERFORMING ORGANIZATION REPORT NUMBER

AFRL-RX-WP-TP-2009-4138

9. SPONSORING/MONITORING AGENCY NAME(S) AND ADDRESS(ES)

Air Force Research Laboratory
Materials and Manufacturing Directorate
Wright-Patterson Air Force Base, OH 45433-7750
Air Force Materiel Command
United States Air Force

10. SPONSORING/MONITORING AGENCY ACRONYM(S)

AFRL/RXLMN

11. SPONSORING/MONITORING AGENCY REPORT NUMBER(S)
AFRL-RX-WP-TP-2009-4138

12. DISTRIBUTION/AVAILABILITY STATEMENT
Approved for public release; distribution unlimited.

13. SUPPLEMENTARY NOTES

14. ABSTRACT

Strategies are described for microstructure-sensitive computational methods for estimating variability of high cycle fatigue (HCF) crack formation and early growth in metallic polycrystals to support design of fatigue resistant alloys. We outline a philosophy of employing computational simulation to establish relations between remote loading conditions and microstructure-scale slip behavior in terms of Fatigue Indicator Parameters (FIPs) as a function of stress amplitude, stress state and microstructure, featuring calibration of mean experimental responses for known microstructures. Effects of process history (carburization and shot peening) and resulting residual stresses are considered in the case of subsurface crack formation at primary inclusions in martensitic steel. The need to characterize extreme value correlations of microstructure attributes coupled to the local driving force (i.e., features) for HCF crack formation is outlined, along with a strategy involving a set of FIPs relevant to different mechanisms of crack formation.

15. SUBJECT TERMS

microplasticity, microstructure-sensitive modeling, high cycle fatigue, fatigue variability

16. SECURITY CLASSIFICATION OF:

a. REPORT	b. ABSTRACT	c. THIS PAGE
Unclassified	Unclassified	Unclassified

17. LIMITATION OF ABSTRACT:
SAR

18. NUMBER OF PAGES
48

19a. NAME OF RESPONSIBLE PERSON (Monitor)
Reji John

19b. TELEPHONE NUMBER *(Include Area Code)*
N/A

i

Fatigue of Materials: Competing Failure Modes
and Variability in Fatigue Life
Edited by K S. Ravi Chandran et al.

MICROSTRUCTURE-SENSITIVE MODELING OF
HIGH CYCLE FATIGUE

Craig Przybyla[2,3], Rajesh Prasannavenkatesan[1], Nima Salajegheh[1], David L. McDowell[1,2]

[1]GWW School of Mechanical Engineering
[2]School of Materials Science & Engineering
Georgia Institute of Technology, Atlanta, GA 30332-0405 USA

[3]Air Force Research Laboratory
Wright Patterson Air Force Base, Ohio 45433

Keywords: Microplasticity, microstructure-sensitive modeling, high cycle fatigue, fatigue variability

Abstract

Strategies are described for microstructure-sensitive computational methods for estimating variability of high cycle fatigue (HCF) crack formation and early growth in metallic polycrystals to support design of fatigue resistant alloys. We outline a philosophy of employing computational simulation to establish relations between remote loading conditions and microstructure-scale slip behavior in terms of Fatigue Indicator Parameters (FIPs) as a function of stress amplitude, stress state and microstructure, featuring calibration of mean experimental responses for known microstructures. Effects of process history (carburization and shot peening) and resulting residual stresses are considered in the case of subsurface crack formation at primary inclusions in martensitic steel. The need to characterize extreme value correlations of microstructure attributes coupled to the local driving force (i.e., features) for HCF crack formation is outlined, along with a strategy involving a set of FIPs relevant to different mechanisms of crack formation. Surface to subsurface transitions are considered in terms of competing mechanisms in the transition from HCF to very high cycle fatigue (VHCF) regimes.

Introduction

While much previous work in modeling fatigue processes in metallic components has focused on component life estimation, there is increasing interest in designing microstructures with tailored fatigue resistance or components with microstructures that vary spatially in composition and/or heat treatment to achieve enhanced performance. Furthermore, there is great

financial and time pressure to compress overall material development and product design cycles, albeit retaining appropriate characterization of fatigue variability for purposes of design for low probability of failure in the High Cycle Fatigue (HCF) regime. Moreover, there is a need to better understand minimum fatigue life behavior of materials to address expensive, overly conservative early retirement of components.

This push towards reducing insertion time for new or modified materials has brought the notion of *microstructure-sensitive* fatigue analysis to the forefront. There are practical limitations to modeling and simulation, of course. Incomplete understanding of failure mechanisms, dominance of each failure mode, and uncertainty in associated models highlight the continuing importance of experiments in guiding modeling and simulation. Key advances can be realized by populating the probability density of failure modes with a combination of experiments and results from properly calibrated modeling and simulation that considers microstructure effects.

In the HCF regime, microstructure plays a key role. The distribution of cyclic slip is quite heterogeneous in this regime, as is the development and growth of small cracks that interact with local microstructure. The reader is referred to several reviews regarding microstructural fatigue mechanisms [1-2]. Fatigue at the microstructure scale is a complex, evolutionary process with stages of formation and growth that depend on a hierarchy of microstructure features. Undue focus on any one scale from an academic perspective is sometimes misleading, as the ratio of total fatigue life associated with each stage of crack formation and growth depends on microstructure, loading conditions, and stress state [3-8].

It is noted that fatigue is a cascade of processes of crack formation and growth that depends on the hierarchical morphology of phases or grains, as well as the presence of non-metallic inclusions in cast or wrought alloys. For example, cracks may form at matrix-inclusion interfaces, assisted by matrix strain localization associated with interfacial debonding or particle fracture. Moreover, cracks can form via impingement of slip bands on grain or phase boundaries, as in certain dual phase alloys or for ostensibly single phase, solid-solution strengthened alloys with second phase particles near grain boundaries. In practical alloy systems, the nucleation regime is often either bypassed or coupled with debonding or fracture of interfaces between inclusions and matrix or at grain boundaries, or crack formation at existing surface scratches, machining marks, or at near-surface pores or inclusions. The problem then

focuses on the formation of small cracks at micronotches that subsequently propagate as microstructurally small cracks. Eventually, these cracks either arrest (fatigue limit) or grow until they are sufficiently long compared to microstructure scales to facilitate the assumption of propagation in a homogeneous material; for many alloy systems under low amplitude HCF conditions, such cracks must typically be several hundred microns long.

The distribution of localized cyclic plastic deformation in the microstructure (cyclic microplasticity) plays a key role in modeling fatigue resistance. Unlike effective properties such as elastic stiffness, fatigue is manifested by extremal microstructure features that promote slip intensification. Under HCF conditions, the cyclic plastic deformation is highly heterogeneous within the microstructure; a strategy for computational HCF modeling of components that must last millions of cycles, such as shafts, bearings, and gears, for example, should focus on extreme statistics of potential sites for microplastic strain localization and fracture that drive crack formation. Moreover, the issue of arrest of small cracks that form at isolated sites of cyclic plastic strain intensification is pertinent to the estimation of the fatigue limit. The crack propagation life beyond the candidate point of initial arrest is often inconsequential as a fraction of the component fatigue life. Complicating features of such components include gradient strain fields, sub-surface inclusions, residual stresses due to thermo-mechanical processing, and characterization of potential mechanisms/sites for crack formation.

On the other hand, for finite life design (for example hundreds of thousands of cycles) the distribution of slip processes is less heterogeneous, and in fact may no longer occur in isolated regions. As the applied strain amplitude increases, slip heterogeneity decreases [6]. Still, microstructure plays a role in establishing "connectivity" of slip within the microstructure that provides enhancement of driving force for small crack formation and growth. Accordingly, concepts of percolation limits for microplastic deformation may be introduced, along with the notion of a microstructurally small crack growth regime in which the crack driving force couples strongly with microstructure barriers [1,9-10]. For such cases, both crack formation and small crack propagation can play a key role in life prediction. Moreover, in the small crack regime, the crack tip plasticity is often large scale such that the cyclic plastic zone is not small compared to crack length and also does not conform to isotropic continuum plasticity assumptions.

These kinds of issues are perhaps most fruitfully explored with computational fatigue analyses to develop understanding in view of the difficulty of obtaining statistically significant fatigue crack formation and propagation data from experiments.

2. Computational Methods in Fatigue Modeling

Experiments are typically used to characterize both mean fatigue resistance and scatter in fatigue as a function of microstructure to facilitate tailoring of microstructure to improve component level fatigue resistance.   Recently, there has been an emphasis on applying computational micromechanics [11-12] to hierarchical microstructures (phases, grains, inclusions, etc.) to characterize cyclic plasticity that drives crack formation at microstructure scales. Goals of such studies are varied, and include:

- o Reduction of the number of required experiments to assess scatter in fatigue.
- o Parametric exploration of various fatigue damage mechanisms to support probabilistic approaches or worse case scenarios for fatigue life prediction schemes.
- o Informing microstructure-sensitive parameters in macroscopic cyclic plasticity and fatigue models for structural applications.
- o Sorting out behaviors associated with crack formation, microstructurally small crack growth and long crack growth to support design of fatigue-resistant microstructures and process parameters (cf. [7, 13-14]). This relies more on obtaining proper trends of models rather than absolute accuracy of correlations/predictions.

2.1 Regimes of Cyclic Plasticity

Cyclic plastic strain behavior is generally decomposed into three regimes: elastic shakedown, reversed cyclic plasticity, and plastic ratcheting [15]. Elastic shakedown is defined as the stress or strain level below which there is a cessation of cyclic plasticity. In other words, the condition of elastic shakedown is obtained when plastic deformation occurs during the early cycles but the steady state behavior is fully elastic due to the build-up of residual stresses. Reversed cyclic plasticity is the condition in which the material experiences reversed plastic straining during cycling with no net accumulation of plastic deformation; reversed cyclic plasticity is sometimes referred as plastic shakedown. Plastic ratcheting describes the condition in which the material

accumulates a net directional plastic strain during each cycle. The ratcheting plastic strain increment per cycle is defined as

$$\left(\Delta\varepsilon_{ij}^{p}\right)_{ratch}=\left(\varepsilon_{ij}^{p}\right)\Big|_{\text{End of the cycle}}-\left(\varepsilon_{ij}^{p}\right)\Big|_{\text{Beginning of the cycle}} \qquad (1)$$

The reversed cyclic plastic strain range is given by

$$\left(\Delta\varepsilon_{ij}^{p}\right)_{cyc}=\left(\Delta\varepsilon_{ij}^{p}\right)_{max}\Big|_{\text{Over the cycle}}-\left(\Delta\varepsilon_{ij}^{p}\right)_{ratch} \qquad (2)$$

2.2 Fatigue Indicator Parameters

In view of the complexity of cyclic irreversibility and damage formation in HCF, we introduce the concept of *Fatigue Indicator Parameters* (FIPs) to serve as computable response parameters that can facilitate comparisons of multiple microstructures via parametric studies. Here, we consider two parameter approaches to define FIPs that incorporate combined effects of cyclic shear and normal stress. One such FIP that seeks to describe transgranular crack initiation associated with intense cyclic plastic shear is the Fatemi-Socie [16-17] parameter

$$P_{FS}=\frac{\Delta\gamma_{max}^{p*}}{2}\left(1+K^{'}\frac{\sigma_{max}^{n*}}{\sigma_{y}}\right) \qquad , \qquad (3)$$

where $\Delta\gamma_{max}^{p*}/2$ is the average (nonlocal) maximum cyclic plastic shear strain over a finite volume of material, σ_{max}^{n*} and σ_{y} are the volume average peak stress normal to the plane of $\Delta\gamma_{max}^{p*}/2$ and cyclic yield strength, respectively, and $K^{'}$ is a constant that controls the effect of normal stress. The spatial volume for nonlocal averaging of the quantities in the FIP is the lesser of approximately 1 μm^{3} or ℓ^{3}, where ℓ is the scale of the transition crack length at which the crack grows out of the influence of the microstructure notch root field at which it may have formed. The FS parameter is a shear-based parameter which has demonstrated good capability to model crack initiation in polycrystals under various multiaxial loading conditions [18-19]. This parameter has also been shown by McDowell and Berard [20] to be closely related to the EPFM ΔJ-integral and related ΔCTD [21], as well as strain-based critical plane concepts [18, 22].

Of course, other analogous FIPs can be introduced for other mechanisms of crack formation. Progressive pileup of dislocations in slip bands (Zener mechanism) that impinge on grain or phase boundaries, or upon oxidized inclusion interfaces, can lead to formation and propagation of small cracks in the microstructure.   In fretting fatigue, for example, progressive plastic deformation of surface layers has been shown to contribute significantly to formation and early growth [23] of cracks on the order of grain size under ostensibly HCF conditions. For example, a Zener parameter can be introduced as an indicator of relative potency to form cracks due to pile-up of slip (e.g., slip band) on grain or phase boundaries, i.e.,

$$P_{ZP} = \gamma_{net}^{p*}\left(1 + K_z^{'}\frac{\sigma_{GB}^{n*}}{\sigma_y}\right) \quad (4)$$

where $\gamma_{net}^{p*} = \max\left(n_i\varepsilon_{ij}^{p}m_j\right)$ among all planes with unit tangent and normal vectors **m** and **n**, respectively, is the maximum net plastic shear strain averaged over a finite volume of material, σ_{GB}^{n*} is the average peak stress normal to a boundary segment impinged by slip, and $K_z^{'}$ is a constant that controls the effect of normal stress.

Others have recently employed similar measures at the grain scale as indicators of propensity to form fatigue cracks [11-12]. Manonukul and Dunne [24] have adopted cumulative plastic strain as a measure of driving force to form microstructure cracks in fatigue. The present work employs either a measure of reversed cyclic plastic strain (irreversible slip-driven crack formation) based on steady state cyclic behavior or cumulative directional strain (ratcheting or pileups) to reflect a driving force to form cracks via decohesion in slip bands and Zener cracking, respectively, as summarized in Figure 1 for two polycrystalline alloys.

2.3 Decomposition of Stages of HCF

An operational decomposition of the total fatigue life among stages is given by [5,8]

$$N_T = N_{inc} + N_{MSC} + N_{PSC} + N_{LC} = N_{inc} + N_{MSC/PSC} + N_{LC} \quad (5)$$

where N_{inc} is the number of cycles to incubate (nucleation plus small crack growth through the region of notch root influence) a crack at a "hotspot" within the microstructure with initial length, a_i, on the order of the microstructure attribute at which the crack forms. Assuming an

averaging volume for the relevant FIP that corresponds to incubation at this scale, one may postulate a relation such as $P_{FS} = \tilde{\gamma}_f' \left(2N_{inc}\right)^c$, where $\tilde{\gamma}_f'$ is a fatigue ductility coefficient appropriate to crack formation at the scale considered.

Cycles N_{MSC}, N_{PSC} and N_{LC} represent the number of cycles to propagate the crack(s) in the regimes of microstructurally small (approximately 3-10 times the grain or second phase size/spacing that affects retardation of the crack driving force), physically small, and long crack growth, respectively. The crack driving force is taken to be the cyclic crack tip displacement range, ΔCTD. In HCF, the incubation and MSC/PSC small crack propagation regimes are dominant ($N_{inc} + N_{MSC/PSC}$) in terms of comparing fatigue resistances of different materials and/or microstructures. The ΔCTD-based MSC/PSC growth relation is shown in Figure 2, where G is an irreversibility factor. Micromechanical studies are necessary to capture ΔCTD interactions with microstructure [1, 5, 10, 27-28]. The form of this MSC growth relation does not rely on applicability of small scale yielding in conventional LEFM concepts but incorporates them naturally under conditions for which they are valid.

It is noted that relations for crack formation and growth in the microstructure-scale regime are still in their very early stages. In particular, very little fundamental work has been done to model microstructure-sensitive relations for crack incubation that consider atomic/dislocation level slip interactions and irreversibilities that promote crack extension. However, the basic multistage framework in Eq. (5) and Figure 2, when combined with mechanism-based simulations to describe cyclic plasticity in heterogeneous microstructures, can facilitate exploration of effects of microstructure morphology at various scales on variability in fatigue response, as well as a means of rank-ordering different microstructures with regard to HCF resistance. The philosophy adopted here is that the formulation should be calibrated to mean fatigue behavior of selected microstructures, thereafter providing capability to assess sensitivity of fatigue life predictions to variations of microstructure within the range of microstructures calibrated.

These concepts have been previously applied to hierarchical microstructures of cast A356-T6 Al alloys [5] and Ni-base superalloys [29-31], aimed at either rank ordering attributes or optimizing microstructure for HCF resistance. We next highlight some recent research directions in computational, microstructure-sensitive fatigue methods that consider: (i) coupling

process route with initial residual stress effects on fatigue behavior of primary inclusions in martensitic steels, (ii) extreme value fatigue scenarios in powder metallurgy and wrought Ni base superalloys, and (iii) consideration of surface to subsurface failure mode transitions at nonmetallic inclusions.

3. HCF Crack Formation in Carburized and Shot Peened Martensitic Gear Steel

High strength low carbon martensitic gear steel is a viable candidate material for high performance, reliable transmission systems in aerospace and automotive applications. Microstructure at different length scales (inclusions, precipitates, and composition gradients) affects fatigue crack nucleation and growth in martensitic steels [32-36]; however, efforts to develop computational models that correlate these attributes to variability in fatigue crack formation and microstructurally small crack growth have been limited. Additionally, processing steps such as carburization and shot peening play a crucial role in improving the HCF resistance of martensitic steels. Fatigue crack nucleation in the HCF regime is highly heterogeneous at the grain scale [37]. Due to the hierarchical microstructure of martensite [38-42] and the scales over which process-induced strengthening effects are realized in components, it is quite challenging to develop models that couple process effects and microstructure attributes at different length scales. A hierarchical approach is most suitable and computationally conducive to investigate the coupling of process route with grain scale cyclic plastic deformation phenomena in components.

This study considers Ferrium® C61 alloy gear steel, which is a low carbon martensitic steel [43] developed by Questek Innovations LLC with the composition listed in Table 1 [44]. Thermo-mechanical processing involves carburization at either 950°C, 1000°C or 1050°C, followed by cryogenic treatment in a liquid nitrogen bath to obtain complete martensitic transformation at the surface. This is followed by tempering at 500°C for 1.5 hours to achieve the desired case strength. Surface treatment involves a standard dual shot peening procedure employed by GM power train. Dual peening consists first of a high-intensity application of peening media to maximize and deepen compressive residual stress at the target surface, followed by a less-intense saturation of softer media intended to smooth out asperities and raise the compressive stress at the near surface [44]. The measured residual stress profile after shot peening is shown in Figure 3a. Carburization and tempering with subsequent surface treatment

such as shot peening are intended to improve HCF strength of steel components [45-49]. Increase of the bending fatigue strength of steel gear teeth via carburization and shot peening has been widely utilized in industry [50-56].

Under reversed bending stress with $R_\varepsilon = 0.05$, it is observed that fatigue cracks form at a depth of approximately 200 to 270 microns below surface, as shown in Figure 3b. The location of crack formation is not within the tensile residual stress region. SEM analysis of the fracture surface and its mating surface indicates that the cracks are formed at clusters of inclusions. A single row of Al_2O_3 inclusions (particles 1, 2, 3 and 4) on the tooth fracture surface and the corresponding location of holes on the mating surface are shown for clarity in Figure 3c [44]. The largest particle (#3), about 10 microns in size, is potentially the most favorable site for fatigue crack nucleation [57]. Debonding of particles was observed, with uncracked particles on fracture surface and corresponding holes on the mating surface. Similar observations regarding subsurface fatigue crack initiation in high strength steels have been reported earlier [58-59]. Inclusion clustering observed at the failure initiation site indicates a potential role for inclusion interaction. Furthermore, the gradient of material properties, applied stress and distribution of residual stress all can cooperatively affect subsurface fatigue crack nucleation.

3.1 Modeling Initial Residual Stress Due to Shot Peening and Effects on Potency

During processing, heat treatment (carburization and tempering) and surface treatment (shot peening) introduce compressive residual stress field at and near the surface. Comparatively, the residual stress introduced by carburization and tempering (-100MPa to -300MPa) is much lower than that introduced through shot peening, especially close to the surface layer of the specimen [13, 29 44. 60]. Shot peening effectively induces equi-biaxial compressive in-plane residual stresses at the surface by virtue of plastic deformation. With these observations and idealizations, Prasannavenkatesan et al. [61] developed a simplified scheme to simulate shot peening that is suitable for initializing residual stress distribution prior to conducting fatigue calculations. The scheme was employed to investigate the fatigue crack nucleation potency at damaged primary inclusions (partially debonded and cracked particles) under the influence of compressive residual stresses. Only selective results are presented here; details regarding the FE framework, boundary conditions, applied remote loading, and modeling strategy can be found elsewhere [61-62]. The material model for martensitic steel employed in these simulations employs initially isotropic,

associative rate independent plasticity with a yield function $f\left(\underset{\sim}{\sigma}-\underset{\sim}{\alpha}\right)=\sqrt{\frac{3}{2}\left(\underset{\sim}{S}-\underset{\sim}{\alpha}^{dev}\right):\left(\underset{\sim}{S}-\underset{\sim}{\alpha}^{dev}\right)}$,

where $\underset{\sim}{\alpha}^{dev}$ is the deviatoric part of the back stress tensor and $\underset{\sim}{S}$ is the deviatoric stress tensor; back stress evolution accounts for material work hardening, and is given by $\underset{\sim}{\dot{\alpha}}=c\frac{1}{\sigma_{YS}}\left(\underset{\sim}{\sigma}-\underset{\sim}{\alpha}\right)\dot{\bar{\varepsilon}}^{p}-r\underset{\sim}{\alpha}\dot{\bar{\varepsilon}}^{p}$, where $\dot{\bar{\varepsilon}}^{p}$ is the uniaxial equivalent plastic strain rate, and c and r are material parameters .

Three-dimensional FE simulations are performed by considering a volume element representing the steel matrix (dimensions in microns) with embedded ellipsoidal non-metallic inclusion(s). The steel matrix is modeled as an elastic-plastic material with pure nonlinear kinematic hardening. The inclusion is modeled as isotropic, linear elastic. Case hardening (carburization and tempering) is considered by varying the material properties from surface to core in accordance with characteristic measured profiles of carbon content. Compressive residual stresses were induced in the volume element corresponding to experimentally measured values at each selected depth below surface, followed by three cycles of loading (strain controlled, R_{ε} = 0.05). The nonlocal (average) value of the Fatemi-Socie parameter $P_{FS}\left(=\Delta\Gamma\right)$ calculated in the proximity of the inclusion is considered as a FIP to facilitate comparison of potency to form fatigue cracks at each subsurface depth as a function of inclusion size. The averaging volume used to compute the nonlocal FIP is 1 μm^{3} [61, 63], selected as the volume that maximizes the computed FIP over all such volumes in the vicinity of the notch root. Cyclic bending stress is applied along the Z direction and the initial equi-biaxial residual stresses act in the X-Z plane.

The variation of $\Delta\Gamma$ with depth for the cases of a single cracked particle and single partially debonded particle are presented in Figures 4 and 5, respectively. In addition to $\Delta\Gamma$, the maximum range of plastic shear strain averaged over 1 μm^{3} at the notch root is presented. The simulation results indicate a strong propensity for crack formation at subsurface depths in accordance with experiments. Detailed parametric studies [61] have investigated the effects of inclusion spacing, size and orientation, with predicted trends for critical depth of the site of crack incubation and early growth consistent with experiments. Further, Zhang et al. [62] performed a series of three-dimensional FE simulations considering realistic distributions of non-metallic inclusions and the results agreed with experimental observations. Shot peening suppresses the

fatigue crack driving force at the surface and shifts the critical crack nucleation site to subsurface depths. The critical depth was observed to show strong dependence on residual stress distribution, applied stress, and property gradients. Comparing results for a single cracked particle (Figure 4) with results for a single partially debonded inclusion (Figure 5), it is observed that the partially debonded particle exhibits a worst case scenario for fatigue crack formation and early growth. Furthermore, predicted depths of subsurface crack nucleation at inhomogeneities such as pores and low stiffness inclusions (sulfide particles) were shown to differ from those of high stiffness inclusions.

4. Extreme Value Statistics of Fatigue Crack Formation in Ni-base Superalloys

Ni-base superalloys are extensively used in aircraft gas turbine engines due to their high strength and creep resistance at high temperatures, conferred by coherent γ' Ni$_3$Al precipitates. Commonly, fatigue crack formation and early growth in these superalloys has been linked to the existence of process-induced defects such as pores or nonmetallic inclusions [63-65]. As processing techniques improve, cleaner Ni-base superalloys are being developed with fewer defects, increasing the probability of crystallographic crack nucleation. For example, Jha et al. [66] noted that the frequency of subsurface fatigue crack initiation dominated surface initiation sites in René 88DT, particularly at lower stress amplitudes in the HCF regime and the transition to the very High Cycle Fatigue (VHCF) regime; here, the nucleation area associated with the size of the crystallographic facets at the sites of fatigue crack formation was observed to be much larger then the average grain size. This suggests that cracks tended to form in larger grains. In the same alloy, Miao et al. [67] noted that the most critical, life limiting fatigue cracks in the HCF/VHCF regimes initiated crystallographically in the subsurface. The grains in which these cracks formed were observed to be large relative to the average grain size. In addition, these grains were associated with higher Schmid factors, indicating they were oriented favorably for slip. Further work on this same material by Shyam et al. [68] also noted that cracks formed predominantly in larger grains or at inclusions near large grains in other HCF fatigue experiments for René 88DT. In addition to this work, others have found that slip bands associated with shearing of the second phase γ' precipitates and subsequent fatigue damage formation have been observed to be more common in coarser grained superalloys, while deformation in the smaller grains has been observed to be more homogeneous [69-70].

4.1 Extreme Value Marked Correlation Functions

The objective is to link the extreme values of FIPs to the key microstructure attributes that are associated with these rare events. Accordingly, a statistical framework should meet three primary requirements:

1) It should contain information regarding both the distributions of microstructure attributes and potential interactions or correlations between multiple microstructure attributes.

2) It must link the distributions of microstructure attributes and correlations between various microstructure attributes to distributions of local response parameters (e.g., FIPs).

3) It must be able to address the extreme value nature of fatigue crack formation and growth scenarios.

A statistical framework that meets these requirements consists of two parts. Given a window Ω we define the probability distribution of the extreme valued response parameter α as $F^{ex}(\alpha|\Omega)$, which is the probability that the response parameter of value α is the extreme value for a sampled statistical volume element of microstructure Ω. This follows the ideas of extreme value sampling from classical extreme value statistics of Gumbel [71-72]. Corresponding to the probability distribution of the extreme value response parameter is the extreme value marked radial correlation function, $R^{\max(\alpha)}(\beta, \beta' \,|\, r, \Omega)$. We define $R^{\max(\alpha)}(\beta, \beta' \,|\, r, \Omega)$ as the probability of finding of a sphere centered at the microstructure attribute β corresponding to the location of the maximum response parameter α in the microstructure window Ω, with microstructure attribute β' at a distance within r to $r + dr$ from β in any direction. Although based on the notion of the marked correlation functions introduced by Pryz [73], this new construct is fundamentally unique in its framing of extreme value statistics.

The process of selectively sampling parts of a known distribution to estimate a second unknown distribution falls under the general classification of importance sampling [74]. Here we estimate the extreme value distribution of a parameter by sampling the extrema of several complete distributions of the same parameter associated with a given microstructure that can be constructed via simulation or experiment.

This two part statistical construct captures both the extreme value response of the microstructure as represented by the response parameter α and the biased correlations of

microstructure attributes between β and β' in the neighborhood of the observed extreme values of α in a microstructure window Ω. In this way, spatial correlations are identified between microstructure attributes that have a high probability of existing in the neighborhood of an extreme value response parameter. This sampling is performed on microstructure window Ω and is expected to depend on the size of Ω. The method requires multiple instantiations of Ω to effectively sample both $F^{ex}(\alpha | \Omega)$ and $R^{\max(\alpha)}(\beta, \beta' | r, \Omega)$ to build up the tail of the probability distribution corresponding to extreme value response neighborhoods. Such sampling can require extensive processing time for both simulations and data analysis depending on the complexity of the models being analyzed. Moreover, the number of samples required depends on the response parameter considered and material being analyzed. Analogous experimental information is typically not available.

4.2 Distributions of Fatigue Parameters in IN 100

Simple statistical volume elements (SVEs) of microstructure were constructed for Ni-base superalloy IN 100. Local plasticity on the scale of the grains is estimated via a microstructure-sensitive crystal plasticity model [75-76] with dependence of strength and work hardening on several material length scales. This model has correlated well with experiments in terms of cyclic stress-strain behavior over a range of microstructures at intended disk operating temperature of 650°C [29, 75-78]. In this particular formulation, the γ' precipitates are not explicitly modeled, but the influence of primary, secondary and tertiary γ' precipitates are included through specific state variables, including dislocation density. This model as been formulated as a UserMATerial subroutine for use in the finite element package ABAQUS [79].

Each microstructure instantiation was large enough to be considered as a representative volume element (RVE) in terms of the overall stress-strain response. In other words, the stress-strain response computed from any microstructure instantiation differs little from that of any other. In contrast, the local maximum response of the FIP or response parameter α for each instantiation differs significantly among these instantiations and for that reason they cannot be considered as RVEs for the extreme value response of interest. The size of an RVE for the extreme value response would be untenably large, in general, for tractable simulations. Hence they are termed SVEs. It is noted that these SVEs are constructed based on similar principles as those employed for SERVEs as defined by Swaminathan and Ghosh [80-81]. The ability to

simulate variations in the local response among SVEs enables us to computationally explore the link between microstructure heterogeneity and distributions of the local driving forces to form fatigue cracks.

In this set of simulations, multiple SVEs were generated and each optimized to fit specified orientation, disorientation and grain size distributions. The disorientation distribution was fit to a random Mackenzie [82-83] distribution. A simulated annealing algorithm similar to that of Shenoy [76] was used to optimize the microstructure to fit these target distributions of grain size and disorientation. A random orientation distribution of the grains was imposed. The number of grains in each SVE was allowed to vary during the fitting process. The final number of grains within each SVE typically ranged between 325-375. The grain size distribution was optimized to fit a lognormal distribution, as shown in Figure 6. An average cube root grain size of ~0.0215 mm was imposed such that the mean and standard deviation of the natural logarithm of the grain volume normalized by imposed average grain volume of $1x10^{-5}mm^3$ were 0.0 and 0.7, respectively. A total of 13824 uniformly distributed quadrilateral elements with reduced-integration (type C3D8R) were employed in each SVE, corresponding to about 40 elements per grain. These SVEs were dimensioned 150 microns along each edge. Periodic boundary conditions were applied in all directions. Each SVE was strained uniaxially to a peak strain of 0.5%, which was approximately 80% of the macroscopic yield point. The straining in tension and compression was completely reversed (*i.e.*, R_ε = -1), with a quasistatic strain rate of approximately 0.002 s^{-1} at 650°C. Each simulation was cycled three times to allow for any initial shakedown, and results were extracted over the third complete cycle.

A total of 100 microstructure instantiations were analyzed using FEM. For each instantiation, the Schmid factor was computed for each element. The crystal plasticity model considers both traditional octahedral slip and cuboidal slip [75-76]. Schmid factors for both octahedral and cuboidal slip were computed. The Schmid factor was assessed in two different ways. The *apparent* Schmid factor for the eth element, m_g^e, is based purely on geometry, i.e.,

$m_g^e = \max\left\{\cos\left(\phi^i\right)\cos\left(\lambda^i\right), i = 1...n\right\}$, where ϕ^i is the angle between the ith slip plane normal and loading direction and λ^i is the angle between the ith slip direction and the direction of uniaxial applied stress on the SVE. The total number of slip systems is *n*. The *local* Schmid factor for the eth element, m_s^e, was computed as the ratio between the maximum resolved shear stress from FE

simulations divided by the global SVE uniaxial applied stress, i.e., $m_s^e = \max(\tau_{rss}^i)/\sigma$ for

i=1…n. In contrast to the apparent Schmid factor, the local Schmid factor considers the local stress state as affected by intergranular interactions and microplasticity. The probability distributions of the apparent and local Schmid factors for both octahedral and cuboidal slip are given in Figure 7. It is interesting to note that the local Schmid factor is more broadly distributed than the apparent Schmid factor, apparently owing to interactions and constraints between neighboring grains. It is also observed that the largest local Schmid factor is most likely to occur when cuboidal slip is favored, which is not the case for the apparent Schmid factor. This reinforces that the local Schmid factor is more relevant to extreme value response than the apparent Schmid factor. In all simulations, the Fatemi-Socie FIP was computed from the plastic strain and stress averaged over each element.

The extreme value distribution function $F^{ex}(\alpha|\Omega)) = F^{ex}(FIP|\Omega)$ of the FIP was estimated by sampling the maximum extreme value FIP in each microstructure instantiation. This distribution was estimated based on the distribution of the element average maximum FIPs determined in each SVE over the set of all simulated SVEs. Extreme value FIPs for sample sizes of 25, 50, 75 and 100 simulated SVEs are presented on a log-normal probability plot in Figure 8. From Figure 8, it is apparent that the extreme value distributions of the FIPs are nearly log-normal in character even for smaller sample sizes (e.g., 25). It is also interesting to note that most of the deviation from a true log-normal distribution occurs at the tails of the extreme value distributions. Detailed examination of the local neighborhoods in the vicinity of the extreme value FIPs in selected SVE simulations reveals the potential complexity of interactions of microstructure attributes such as disorientation with slip system deformation mechanisms. For example, local Schmid factors are likely to be larger near grain boundaries due to constraint from neighboring grains. Even in the absence of a single large unfavorably oriented grain, two adjacent grains with hard orientation for octahedral slip can induce high stresses in adjacent grains that are more favorably oriented for octahedral slip, thereby enhancing the FIP substantially.

The second aspect of the proposed statistical framework, $R^{\max(\alpha)}(\beta, \beta'|r, \Omega)$, is illustrated by considering the microstructure attribute "grain orientation". Orientation space has been tessellated into discrete orientation bins; thus, each grain orientation is associated with a

15

particular bin number. Hence, any reference to a particular orientation bin actually denotes a particular orientation that falls within that orientation bin as determined by the tessellation scheme used [84].

The complete radial distribution function and extreme value marked radial distribution function for a few specific orientations are plotted in Figure 9. The complete radial distribution function considers the probabilities of finding a sphere that has one orientation at its center and another (or the same) orientation a distance r to $r + dr$ from the center in any direction. The complete radial distribution function is sampled at each finite element center over the entire ensemble of simulated SVEs. In contrast, the extreme value marked radial distribution function is only sampled starting at the point (or element in this case) in *each* SVE that is associated with the maximum extreme value FIP for that SVE. The specific orientations plotted in Figure 9 were selected because they occurred with a significantly higher probability at the location of the maximum FIP as determined by comparing the extreme value marked radial distribution function to the complete radial distribution functions for orientation. This can be seen by comparing the magnitudes of the complete radial distribution function with the extreme value marked radial distribution function.

In this manner we are able to explore the correlations between different orientations in the regions of extreme value FIPs. First, consider autocorrelations between the same orientations for IN 100. A single component of the extreme value marked radial distribution function, $R^{\max(\alpha)}(g, g' \mid r, \Omega)$, between orientation bin $g = 56$ and itself (i.e., $g' = 56$), is compared to the corresponding component of the *overall* complete radial distribution function of orientation in Figure 9(a). This particular orientation bin can be described by its center point in Euler space at $\varphi_1 = 5.3014$, $\Phi = 1.4107$, and $\varphi_2 = 0.57186$ and has apparent Schmid factors of $m_g^{oct} = 0.3241$ and $m_g^{cub} = 0.4941$ for octahedral and cuboidal slip, respectively. It is seen that the orientation $g = 56$ is much more likely to exist near an extreme value FIP than in the set of overall random microstructure instantiations. Considering Figure 9(a), the probability that orientations $g_1 = 56$ and $g_2 = 56$ will be the same is much higher for distances less than one average grain size. It is expected that vectors shorter than the grain size will have a higher probability of having both their head and tail at the same grain orientation when randomly placed in a microstructure because the orientations within a grain are the same. For distances greater than the average grain

size, the magnitude of $R^{\max(\alpha)}(g,g'|r,\Omega)$ decreases significantly. In words, this represents the probability of finding two grains with the same orientation next to or in close proximity to each other. The probability of finding a vector r whose head and tail are in orientation g = 56 is three times greater at an extreme value FIP in a volume Ω than in the overall ensemble of microstructures when r/d (the length of vector r is normalized by the average cube root grain size $d = 21$ μm) is smaller than about one average grain size. In Figure 10, the probability density of the distribution of local Schmid factors is given for all grains and for two specific orientations. For orientation g = 56, the distribution of the local Schmid factor for cuboidal slip is to the left of the distribution of Schmid factors for octahedral slip. Thus, cuboidal slip appears to be preferred for this particular orientation. When we compare the distributions of Schmid factors for orientation g = 56 and for all the orientations, there is a significantly higher probability that the local Schmid factor for cuboidal slip will be larger in g = 56 then in a grain selected at random.

The propensity of cross-correlated orientations to be associated with extreme value FIPS can also be explored. Figure 9(b) presents the probabilities for finding orientations $g = 56$ and $g = 58$ at a distance r/d from each other in both the entire microstructure and at the extreme value FIP sites, respectively. Orientation $g = 58$ is represented by $\varphi_1 = 5.6941$, $\Phi = 1.3952$, and $\varphi_2 = 0.18566$ in Euler space. There is a higher probability that $g = 56$ and $g = 58$ are neighboring grains at an extreme value site than in the overall microstructure. In Figure 9(b), the probability that $g = 56$ and $g = 58$ are located between one and two average grain sizes from each other at an extreme value site is as much as 0.7%. This is much higher than in the overall microstructure (~0.02%). The apparent Schmid factors for orientation $g = 58$ are $m_g^{oct} = 0.4746$ and $m_g^{cub} = 0.4426$ for octahedral and cuboidal slip, respectively. From Figure 10, however, we observe that there is a much higher probability for a local Schmid factor with greater magnitude for cuboidal slip than for octahedral slip, suggesting that cuboidal slip dominates in this orientation even though the apparent Schmid factor may suggest the contrary. It appears that these simulations indicate that grains or clusters of grains oriented for favorable cuboidal slip are associated with the extreme value FIP, but more work is needed to validate these results. It is particularly important to compare these findings with experimental results to ensure proper calibration of the model assumptions regarding mechanisms.

In fact, development of algorithms for sorting through the large datasets involving correlations and cross-correlations is challenging in its own right. Furthermore, modeling and

simulation imposes certain assumptions and idealizations regarding deformation modes that can bias extreme value correlations. For example, in the case of IN 100, the influence of cube slip at 650°C is generally thought to be small. Physically, cube slip is a manifestation of zig-zag cross slip of octahedral systems in confined volumes, for example between precipitates [85]. The continuum approximation employed in the present work considers cube slip as an accommodational deformation mode for hard crystallographic orientations in terms of conventional octahedral slip. If the material models underlying the overall framework change, then so do spatial correlations at extreme value hotspots. Accordingly, it is emphasized that experimental results must be used to corroborate predictions of characteristics of extreme value fatigue crack initiation sites to ensure that predicted trends concur with reality. On the other hand, it is clear that enormous numbers of physical experiments would be necessary to characterize the tails of the distributions for rare event fatigue crack initiation in HCF. Moreover, from a practical perspective there are limitations on experimental sampling of the details of crack initiation sites due to degradation and evolution of microstructure after cracks have formed and propagated. It seems likely that a combined computational-experimental approach to this problem is most practical and time/cost efficient. The role of the analyst/designer is to employ properly calibrated and verified models in such a framework.

5. Fatigue Failure Mode Transition: Surface versus Bulk Inclusions

Primary inclusions are often dominant sites of fatigue crack formation and early growth in high strength steels, powder metallurgy alloys, and casting alloys. Transition from surface-dominated fatigue processes to subsurface failure initiation is often observed in these systems in the transition from HCF (10^6 cycles) to the VHCF regimes (10^9 cycles and beyond) [86-87]. Competition between near surface and bulk inclusions is key to this failure mode transition. Cashman [88] studied competing fatigue failure modes for René 95, with nucleation attributed to the presence of small ceramic inclusions; the difference in fatigue lives was an order of magnitude between surface and subsurface initiated modes of failure. Jha et al. [89-90] noted the separation of experimental fatigue life data into two distinct populations corresponding to competing surface and bulk initiation at nonmetallic particles, considering two aircraft gas turbine engine materials, a titanium alloy, and a Ni-base superalloy. The increased scatter in the experimental life data [91-93] in clean steels at low stress amplitudes is attributed to the

competition between surface and internal inclusion failure modes that manifest significantly different fatigue lives.

5.1 Potential Influence of a Protective Surface Oxide Layer

At a given stress amplitude, limited experimental fatigue life data are most appropriate for estimation of mean behavior of each population corresponding to surface and internal failure nucleation. Accurate assessment of the ratio of the number of surface to internal nucleation events (surface versus internal nucleation probability) could be used to effectively improve the assessment of the mean life of the entire population; the latter is otherwise intractable to estimate via experiments since it is highly sensitive to slight variation in the number of life data in each population. Probabilistic approaches based on the Poisson distribution of microstructure hotspots within the fatigue specimen are appropriate for studying specimen size dependence as the probability of having a detrimental microstructure attribute in the bulk of specimen increases in larger specimens; however, such approaches are not fully mechanistic and fail to capture the decrease in surface relative to internal nucleation probability with decreasing stress level. Among other parameters, cooperative influence of environment through the formation of protective surface oxide layer and specimen size are suspected to significantly influence the surface versus internal nucleation probabilities. Mechanically intact surface oxide scales can form at elevated temperatures due to dynamic equilibrium of continuous microcracking with superimposed oxide-healing processes [94]. The oxidation behavior of metallic alloys is complex due to the interplay between heterogeneous oxide growth, oxide interaction, oxide volatilization, and spalling. At low stress amplitudes, a protective oxide layer may form which can endure the applied stress; this is supported by the observation of a strain threshold in a Ni-base superalloy below which inherent scale flaws do not form through-thickness cracks [95]. Plasticity of the surface oxide layer at elevated temperatures may also assist in maintaining a continuous surface oxide layer [96]. The protective oxide layer may alter the driving forces for fatigue crack nucleation from surface and internal inclusions in a disproportionate manner, causing a change in surface versus bulk nucleation probabilities as a function of bulk stress amplitude. For N18 PM Ni-base superalloy, de Bussac [97] has shown that the probability of surface initiation decreased by over a factor of two as the applied strain decreased from 0.4% to 0.35%.

In this study, parametric finite element simulations are performed using ABAQUS 6.6 [79] to assess the influence of an intact stiff surface oxide layer on the potency of near surface partially debonded spherical inclusions to nucleate fatigue cracks at various depths from the free surface. Generalized plane strain 2-D finite element simulations are conducted assuming isotropic linear elastic non-metallic inclusions embedded in an elasto-plastic matrix with nonlinear kinematic hardening constitutive relations [98]. The matrix material in this study is representative of martensitic steel, employing the same model outlined in Section 3. The surface oxide layer is considered to be linear elastic with an elastic modulus of 400 GPa, corresponding to that of alumina [96]. Relevant mechanical properties are listed in Table 2.

Figure 11 shows the influence of a one-micron-thick surface oxide layer on the P_{FS} FIP for spherical inclusions with diameter of 10 μm located at various depths from the free surface. In this case, the depth is defined as the minimum distance of the inclusion edge from the surface. Near surface inclusions are most affected by the oxide layer; their potency for nucleating fatigue cracks decreases by more than 20% as the oxide thickness builds up to 1 μm. In practice, cracks that form at near surface inclusions often propagate rapidly toward the surface, effectively increasing the size of the initiating defect. Thus, they should be classified as surface failures even though they lie below the specimen surface. Suppression of nucleation potency of near surface inclusions by the oxide layer will result in lower surface nucleation probability and contribute to the apparent surface (HCF) to bulk (VHCF) transition in fatigue crack nucleation sites at decreasing stress amplitudes for which the oxide layer is less likely to rupture or spall. In an analogous manner, surface coatings can also enhance the mean fatigue behavior of such alloys when inclusions control the fatigue life. Of course, detailed analyses of oxidation processes, stresses and failure modes of oxide layers raise complex issues in their own right, but are necessary to quantify effects of periodic overloads or to predict the thickness at which oxide fracture or spallation might occur.

It can be surmised that several competing processes affect the stress amplitude dependence of the surface to subsurface transition of fatigue crack formation and early growth. For instance, nucleation potency of a near surface inclusion decreases as the oxide layer grows as shown in Figure 12. However, the average defect size that forms in the oxide scale during scale growth increases along with the probability of scale failure [95], providing an opposing influence on the net probability of surface to bulk fatigue failure nucleation. In addition, size effects of

inclusions relative to local microstructure (e.g., grain size) play a role in the stress amplitude dependence of the probabilities of surface versus subsurface failures.

5.2 Weighted Probabilities for Surface Versus Subsurface Fatigue Crack Formation

Prediction of the ratio of surface to subsurface probabilities for crack initiation demands a probabilistic-mechanics framework that incorporates competing effects of local microstructure neighborhoods, proximity to the surface, inclusion size and shape, and interaction with surface oxides or other environmental effects. As the stress amplitude decreases, the influence of microstructure attributes becomes pronounced since microplasticity dominates. The probability of having life limiting hotspot microstructure configurations in the bulk of the specimen for fatigue crack formation and early growth increases with decreasing applied stress even though the bulk to surface volume remains constant [94]. As the applied stress amplitude decreases, the number density of microstructure hotspots that can produce sufficient driving force for fatigue crack nucleation decreases and so does the probability of having a hotspot in the surface relative to bulk. For example, at stress amplitudes σ_{1a} and σ_{2a} for a given applied R ratio, an average number density of microstructure configurations, Ψ_1 and Ψ_2 can produce sufficient driving force for fatigue crack nucleation such that if $\sigma_{1a} > \sigma_{2a}$, then $\Psi_1 > \Psi_2$ and

$$\frac{P_f^{\text{Surface}}}{P_f^{\text{Bulk}}}\bigg|_{\sigma_a} \approx \frac{1 - P_f^{\text{Bulk}}\big|_{\sigma_a}}{P_f^{\text{Bulk}}\big|_{\sigma_a}} = \frac{1 - \left(\dfrac{V^{\text{Bulk}}}{V^{\text{Total}}}\right)^{\Psi}}{\left(\dfrac{V^{\text{Bulk}}}{V^{\text{Total}}}\right)^{\Psi}}$$

$$\left(\frac{V^{\text{Bulk}}}{V^{\text{Total}}} < 1, \Psi_1 > \Psi_2\right) \quad \rightarrow \quad \frac{P_f^{\text{Surface}}}{P_f^{\text{Bulk}}}\bigg|_{\sigma=\sigma_{1a}} > \frac{P_f^{\text{Surface}}}{P_f^{\text{Bulk}}}\bigg|_{\sigma=\sigma_{2a}}$$

(6)

The essential notion used to describe the stress amplitude dependence of the failure mode transition from HCF to VHCF regimes is the weighting of the probability of finding microstructure attributes of a certain size, shape, and spatial correlation with other microstructure attributes by the corresponding potency of forming fatigue cracks. In effect, this is entirely analogous to the use of the marked correlation function in Section 4 to identify the extreme value statistics for HCF in microstructures with complex, multivariate interactions. Work is underway

to pursue the description of the HCF to VHCF failure mode transition illustrated schematically in Figure 13.

6. Conclusions

Certain underdeveloped elements of microstructure-sensitive computational methods are outlined and discussed for estimating effects of process route and microstructure on variability of crack formation and early growth in the HCF regime for a wide range of alloy systems. The concept of microplasticity within individual grains is introduced as a key driving force parameter for HCF resistance and variability of response, and associated Fatigue Indicator Parameters (FIPs) are introduced that relate to grain scale crack formation and microstructurally small fatigue crack growth. Approaches are introduced for incorporating effects of process history on initial residual stress at notches and second phase primary inclusions, with application to martensitic steels and PM Ni-base superalloys. Novel methods are introduced for characterizing extreme value "hotspots" that govern the low probability of failure regime in HCF; they can be summarized as the introduction of weight factors based on the extreme values of values of FIPs in spatial correlations between attributes that ostensibly drive fatigue failure (e.g., inclusions, pores, large grains) and other attributes in the neighborhood of these locations. To this end, marked correlation functions are introduced to explore biased or weighted spatial correlations of microstructure attributes (e.g., grain size and orientation) in the neighborhood of hotspots in Ni-base superalloys. Surface to subsurface transitions are considered in terms of competition between surface proximity of primary inclusions and potential protective effects of oxides as applied stress amplitude decreases. Such weighted probability methods depart from conventional approaches that consider only stereological characterization of attributes and extreme value spatial correlations of such geometric attributes. In other words, it is not enough to simply quantitatively characterize the microstructure – companion simulations of responses are necessary to demarcate regions of interest. In the HCF regime, companion experiments are costly and often ambiguous in terms of supporting correlation of fatigue crack initiation sites with microstructure anomalies, a problem analogous to "finding a needle in a haystack." Judicious modeling and simulation can assist in filling this gap in design of process histories and microstructures to enhance fatigue resistance or mitigate microstructure-related fatigue issues.

Acknowledgments

References

[1]   McDowell, D.L. Basic issues in the mechanics of high cycle metal fatigue. International Journal of Fracture 1996; 80:103-145.

[2]   Suresh, S. <u>Fatigue of Materials</u>. Cambridge University Press, 2nd Ed., Cambridge, UK, 1998.

[3]   Venkataraman, G., Chung, Y.W. and Mura, T. Application of minimum energy formalism in a multiple slip band model for fatigue - II. Crack nucleation and derivation of a generalized Coffin-Manson law. Acta Metallurgica Materialia 1991; 39(100:2631-2638.

[4]   Repetto, E.A. and Ortiz, M. A micromechanical model of cyclic deformation and fatigue crack nucleation in F.C.C. single crystals. Acta Materialia 1997; 45(6):2577-2595.

[5]   McDowell, D.L., Gall, K., Horstemeyer, M.F. and Fan, J. Microstructure-based fatigue modeling of cast A356-T6 alloy. Engineering Fracture Mechanics 2003; 70:49-80.

[6]   Bennett, V.P. and McDowell, D.L. Polycrystal orientation distribution effects on microslip in high cycle fatigue. International Journal of Fatigue 2003; 25:27-39.

[7]   McDowell, D.L. Microstructure-sensitive computational fatigue analysis. Handbook of Materials Modeling, Part A: Methods, eds. Sidney Yip and M.F. Horstemeyer, Springer, the Netherlands, 2005:1193-1214.

[8]   McDowell, D.L. Simulation-based strategies for microstructure-sensitive fatigue modeling. Materials Science and Engineering A. 2007; 468-470:4-14.

[9]   Bennett, V.P. and McDowell, D.L. Crystal plasticity analyses of stationary, microstructurally small surface cracks in ductile single phase polycrystals. Fatigue and Fracture of Engineering Materials and Structures 2002; 25(7):677-693.

[10]   Bennett, V.P. and McDowell, D.L. Crack tip displacements of microstructurally small surface cracks in single phase ductile polycrystals. Engineering Fracture Mechanics 2003; 70:185-207.

[11]   Dang-Van, K. Macro-micro approach in high-cyclic multiaxial fatigue. In: McDowell DL, Ellis R, editors. Advances in Multiaxial Fatigue, ASTM STP 1191. Philadelphia: ASTM; 1993:120–30.

[12]   Papadopoulos, I.Y. High cycle fatigue criterion applied in biaxial and triaxial out-of-phase stress conditions. Fatigue and Fracture of Engineering Materials and Structures 1995; 18(1):79–91.

[13]   Olson, G.B. Designing a new material world. Science, 2000; 288:993-998.

[14]   McDowell, D.L. Materials design: a useful research focus for inelastic behavior of structural metals. Special Issue of the Theoretical and Applied Fracture Mechanics, Prospects of Mesomechanics in the 21st Century: Current Thinking on Multiscale Mechanics Problems, eds. G.C. Sih and V.E. Panin, 2001; 37:245-259.

[15]   Ambrico, J.M. and Begley, M.R. Plasticity in fretting contact. Journal of the Mechanics and Physics of Solids 2000; 48(11):2391-2417.

[16]   Fatemi, A. and Socie, D.F. Critical plane approach to multiaxial fatigue damage including out-of-phase loading. Fatigue and Fracture of Engineering Materials & Structures 1988; 11(3):149-165.

[17]   Fatemi, A. and Kurath, P. (1988). Multiaxial fatigue life predictions under the influence of mean-stresses. Journal of Engineering Materials and Technology, Transactions of the ASME 1988; 110(4): 380-388.

[18]   Socie, D.F. Critical plane approaches for multiaxial fatigue damage assessment. In: Advances in Multiaxial Fatigue, eds D.L. McDowell and R. Ellis. ASTM STP 1191, ASTM, Philadelphia, 1993:7–36.

[19]   McDowell, D.L. Multiaxial fatigue strength. ASM Handbook, Vol. 19 on Fatigue and Fracture, ASM International, 1996:263-273.

[20]   McDowell, D.L. and Berard, J.-Y. A ΔJ-based approach to biaxial fatigue. Fatigue and Fracture of Engineering Materials and Structures. 1992; 15:719-741.

[21]   McDowell, D.L. and Bennett, V.P. Micromechanical aspects of small multiaxial fatigue cracks, Proc. 5th Int. Conf. On Biaxial/Multiaxial Fatigue & Fracture, Cracow, Poland, 1997:325-348.

[22]   Brown, M. and Miller, K.J. A theory for fatigue failure under multiaxial stress-strain conditions. Proceedings of the Institution of Mechanical Engineers 1973; 187(65):745-755.

[23]   Goh, C.-H., Neu, R.W. and McDowell, D.L. Influence of Nonhomogeneous Material in Fretting Fatigue, ASTM STP 1425, Fretting Fatigue: Advances in Basic Understanding and Applications, 2002:183-205.

[24]   Manonukul, A. and Dunne, F.P.E. High- and Low-Cycle Fatigue Crack Initiation Using Polycrystal Plasticity, Proceedings of the Royal Society London A. 2004; 460(2047):1881-1903.

[25]   Le Biavant, K., Pommier, S. and Prioul, C. Local texture and fatigue initiation in a Ti-6Al-4V titanium alloy. Fatigue and Fracture of Engineering Materials and Structures 2002; 25:527-545.

[26]   Morrison, D.J. and Moosbrugger, J.C. Effects of grain size on cyclic plasticity and fatigue crack initiation in nickel. International Journal of Fatigue 1997; 19:S51-S59.

[27]   Li, C. Vector CTD analysis for crystallographic crack growth. Acta Metallurgica et Materialia 1990; 38(11):2129–2134.

[28]   Fan, J., McDowell, D.L., Horstemeyer, M.F. and Gall, K. Computational micromechanics analysis of cyclic crack-tip behavior for microstructurally small cracks in dual-phase Al-Si alloys. Engineering Fracture Mechanics 2001; 68:1687-1706.

[29]   Shenoy, M.M., Zhang, J. and McDowell, D.L. Estimating fatigue sensitivity to polycrystalline Ni-base superalloy microstructures using a computational approach. Fatigue and Fracture of Engineering Materials and Structures 2997; 30(10):889-904.

[30]   Shenoy, M., Tjiptowidjojo, Y. and McDowell, D.L. Microstructure-sensitive modeling of polycrystalline IN 100. International Journal of Plasticity 2008; 24:1694–1730.

[31]   McDowell, D.L. Viscoplasticity of heterogeneous metallic materials. Materials Science and Engineering R: Reports 2008; 62(3):67-123.

[32]   Krauss, G. Deformation and fracture in martensitic carbon steels tempered at low temperatures. Metallurgical and Materials Transactions A: Physical Metallurgy and Materials Science. 2001; 32(4):861-877.

[33]   Krauss, G. Martensite in steel: strength and structure. San Carlos de Bariloche, Argentina: Elsevier; 1999:40-57.

[34]   Krauss, G. Microstructure and performance of carburized steel. Part I: martensite. Advanced Materials and Processes 1995; 147(5):40-40.

[35]   Shin, J.-C., Lee, S. and Ryu, J.H. Correlation of microstructure and fatigue properties of two high-strength spring steels. International Journal of Fatigue 1999; 21(6):571-579.

[36]   Zaccone, M.A., Kelley, J.B. and Krauss, G. Strain hardening and fatigue of simulated case microstructures of carburized steels. Industrial Heating 1989; 56(9):7.

[37]   Morrissey, R., Goh, C.-H. and McDowell, D.L. Microstructure-scale modeling of HCF deformation. Mechanics of Materials 2003; 35(3-6):295-311.

[38]   Marder, A.R. and Krauss, G. Formation of low carbon martensite in Fe-C alloys. ASM Transactions Quarterly 1969; 62(4):957-964.

[39]   Marder, A.R. and Krauss, G. Morphology of martensite in iron-carbon alloys. American Society of Metals -- Trans. 1967; 60(4):651-660.

[40]   Kitahara, H., Ueji, R., Tsuji, N. and Minamino, Y. Crystallographic features of lath martensite in low-carbon steel. Acta Materialia 2006; 54(5):1279-1288.

[41]   Morito, S., Saito, H., Ogawa, T., Furuhara, T. and Maki, T. Effect of austenite grain size on the morphology and crystallography of lath martensite in low carbon steels. ISIJ International 2005; 45(1):91-94.

[42]   Morito, S., Yoshida, H., Maki, T. and Huang, X. Effect of block size on the strength of lath martensite in low carbon steels. Materials Science and Engineering A 2006; 438-440(SPEC ISS):237-240.

[43]   Kuehmann, C.J. and Olson, G.B. Gear steels designed by computer. Advanced Materials and Processes 1998; 153(5):40-43.

[44]   Tiemens, B.L. Performance optimization and computational design of ultra-high strength gear steels. Department of Materials Science and Engineering, PhD Thesis, Northwestern University, Evanston, IL, 2006.

[45]   Ceschini, L. and Minak, G. Fatigue behaviour of low temperature carburised AISI 316L austenitic stainless steel. Surface and Coatings Technology 2008; 202(9):1778-1784.

[46]   Tokaji, K. and Akita, M. Effect of carburizing on notch fatigue behaviour in AISI 316 austenitic stainless steel. Surface and Coatings Technology 2006; 200(20-21):6073-6078.

[47]   Farfan, S., Rubio-Gonzalez, C., Cervantes-Hernandez, T. and Mesmacque, G. High cycle fatigue, low cycle fatigue and failure modes of a carburized steel. International Journal of Fatigue 2004; 26(6):673-678.

[48]   Kawagoishi, N., Nagano, T. and Moriyama, M. Effect of shot peening on fatigue strength of maraging steel. Sixth International Conference on Computer Methods and Experimental Measurements for Surface Treatment Effects Crete, Greece: WITPress, Southampton, United Kingdom; 2003; 99-108.

[49]   Iwata, N., Tomota, Y., Katahira, K. and Suzuki, H. Effect of shot peening on fatigue fracture for an as quenched martensitic steel. Materials Science and Technology 2002; 18(6):629-632.

[50]   Brown, J. Shot peening increases gear life. Power Transmission Design 1996; 38(5):61-64.

[51]   Benedetti, M., Fontanari, V., Hohn, B.R., Oster, P. and Tobie, T. Influence of shot peening on bending tooth fatigue limit of case hardened gears. International Journal of Fatigue 2002; 24(11):1127-1136.

[52]   Almen, J.O. Fatigue weakness of surfaces. Product Engineering 1950; 21(11):117-140.

[53]   Sieber, R. Bending fatigue performance of carburized gear steels. Detroit, MI, USA: Publ by SAE, Warrendale, PA, USA 1992; 1-18.

[54]   Freborg, A.M., Ferguson, B.L., Li, Z., Schwam, D.X. and Smith, B.J. Bending fatigue strength improvement of carburized aerospace gears. Phoenix, AZ, United States:

American Helicopter Society, Alexandria, VA 22314-2538, United States 2006; 2092-2102.

[55]   Krug, T., Lang, K.H., Fett, T. and Lohe, D. Influence of residual stresses and mean load on the fatigue strength of case-hardened notched specimens. Materials Science and Engineering A 2007; 468-470:158-163.

[56]   Inoue, K. and Kato, M. Estimation of fatigue strength enhancement for carburized and shot-peened gears. Journal of Propulsion and Power 1994; 10(3):362-368.

[57]   Murakami, Y. and Endo, T. Effects of small defects on fatigue strength of metals. International Journal of Fatigue 1980; 2(1):23-30.

[58]   Toyoda, T., Matsui, T. and Murakami, Y. A Study of Inclusions Causing Fatigue Cracks in Steels for Carburized and Shot Peened Gears. JSAE Review 1990; 11:50-54.

[59]   Shiozawa, K. and Lu, L. Very high-cycle fatigue behaviour of shot-peened high-carbon-chromium bearing steel. Fatigue and Fracture of Engineering Materials and Structures 2002; 25(8-9):813-822.

[60]   Xiao, H., Chen, Q., Shao, E., Wu, D., Chen, Z. and Wang, Z. The effect of shot peening on rolling contact fatigue behaviour and its crack initiation and propagation in carburized steel. Wear 1991; 151(1):77-86.

[61]   Prasannavenkatesan, R., Zhang, J., McDowell, D.L., Olson, G.B. and Jou, H.-J. 3D modeling of subsurface fatigue crack nucleation potency of primary inclusions in heat treated and shot peened martensitic gear steels. International Journal of Fatigue 2008 (in review).

[62]   Zhang, J., Prasannavenkatesan, R., Shenoy, M. and McDowell, D.L. Modeling fatigue crack nucleation potency at primary inclusions in carburized and shot-peened martensitic steel. Engineering Fracture Mechanics 2008; doi:10.1016/j.engfracmech.2008.10.011.

[63]   Prasannavenkatesan, R., McDowell, D.L., Olson, G.B. and Jou, H.-J. Modeling effects of compliant coatings on HCF resistance of primary inclusions in high strength steels. Journal of Engineering Materials and Technology, Trans. ASME 2008(in review)

[64]   Hyzak, J.M. and Bernstein, I.M. The effect of defects on the fatigue crack initiation process in 2 p/m super-alloys. 1. Fatigue origins. Metallurgical Transactions a-Physical Metallurgy and Materials Science 1982; 13:33-43.

[65]   Goto, M. and Knowles, D.M. Initiation and propagation behaviour of microcracks in Ni-base superalloy Udimet 720 Li. Engineering Fracture Mechanics 1998; 60:1-18.

[66]   Pang, H.T. and Reed, P.A.S. Fatigue crack initiation and short crack growth in nickel-base turbine disc alloys-the effects of microstructure and operating parameters. International Journal of Fatigue 2003; 25:1089-1099.

[67]   Jha, S.K., Caton, M.J., Larsen, J.M., Rosenberger, A.H., Li, K. and Porter, W.J. Superimposing mechanisms and their effect on the variability in fatigue lives of a nickel-based superalloy. In: Materials Damage Prognosis, J. M. Larsen, L. Christodoulou, J. R. Calcaterra, M. L. Dent, M. M. Derriso, W. J. Hardman, J. W. Jones, and S. M. Russ, Eds.: TMS (The Minerals, Metals and Materials Society), 2005.

[68]   Miao, J., Pollock, T.M. and Jones, J.W. Very high cycle fatigue behavior of nickel-based superalloy René 88DT at 593°C. In: VHCF-4: Fourth International Conference on Very High Cycle Fatigue, Ann Arbor, Michigan, USA 2007.

[69]   Shyam, A., Torbet, C.J., Jha, S.K., Larsen, J.M., Caton, M.J., Szczepanski, C.J., Pollock, T.M. and Jones, J.W. Development of ultrasonic fatigue for rapid, high temperature fatigue studies in turbine engine materials. Champion, PA, United States 2004; 259-268.

[70]   Antolovich, S.D. and Jayaraman, N. Metallurgical instabilities during the high-temperature low-cycle fatigue of nickel-base super-alloys. Materials Science and Engineering 1983; 57:L9-L12.

[71]   Lerch, B.A., Jayaraman, N. and Antolovich, S.D. A study of fatigue damage mechanisms in Waspoloy from 25°C to 800°C. Materials Science and Engineering 1984; 66:151-166.

[72]   Gumbel, E.J. Statistics of extremes. New York: Columbia University Press, 1958.

[73]   Castillo, E. Extreme value theory in engineering. Boston: Academic, 1988.

[74]   Pyrz, R. Correlation of microstructure variability and local stress-field in two-phase materials. Materials Science and Engineering A-Structural Materials Properties Microstructure and Processing 1994; 177:253-259.

[75]   Bucklew, J.A. Introduction to Rare Event Simulation. New York: Springer, 2004.

[76]   Shenoy, M.M. Constitutive modeling and life prediction in Ni-base superalloys. PhD Thesis, Georgia Institute of Technology, Atlanta, GA 2006.

[77]   Wang, A.-J., Kumar, R.S., Shenoy, M.M. and McDowell, D.L. Microstructure-based multiscale constitutive modeling of γ - γ' nickel-base superalloys. International Journal of Multiscale Computational Engineering 2006; 4(5-6):663-692.

[78]   Shenoy, M.M., Kumar, R.S. and McDowell, D.L. Modeling effects of nonmetallic inclusions on LCF in DS nickel-base superalloys. International Journal of Fatigue 2005; . 27:113-127.

[79]   ABAQUS 6.6. Providence, RI, Simulia, 2006.

[80]   Swaminathan, S., Ghosh, S. and Pagano, N.J. Statistically equivalent representative volume elements for unidirectional composite microstructures: Part I - without damage. Journal of Composite Materials 2006; 40:583-604.

[81]   Swaminathan, S. and Ghosh, S. Statistically equivalent representative volume elements for unidirectional composite microstructures: Part II - with interfacial debonding. Journal of Composite Materials 2006; 40:605-621.

[82]   Mackenzie, J.K. Second paper on statistics associated with the random disorientation of cubes. Biometrika 1958; 45:229-240.

[83]   Mackenzie, J.K. The distribution of rotation axes in a random aggregate of cubic crystals. Acta Metallurgica 1964; 12:223-225.

[84]   Przybyla, C.P., Adams, B.L. and Miles, M.P. Methodology for determining the variance of the Taylor factor: application in Fe-3%Si. Journal of Engineering Materials and Technology, Trans.ASME 2007; 129:82-93.

[85]   Osterle, W. and Bettge, D. Modeling the orientation and direction dependence of the critical resolved shear stress of nickel-base superalloy single crystals. Acta Materialia 2000; 48:689–700.

[86]   Kanazawa, K. and Nishijima, S. Fatigue fracture of low alloy steel at ultra-high-cycle region under elevated temperature condition. Zairyo/Journal of the Society of Materials Science, Japan 1997; 46(12):1396-1401.

[87]   Nishijima, S. and Kanazawa, K. Stepwise S-N curve and fish-eye failure in gigacycle fatigue. Fatigue and Fracture of Engineering Materials and Structures 1999; 22(7):601-607.

[88]   Cashman, G.T. A Statistical Methodolgy for the Preparation of a Competing Modes Fatigue Design Curve. Journal of Engineering Materials and Technology, Trans. ASME 2007; 129(1): 159-168.

[89]   Jha, S. K., Caton, M.J. and Larsen, J.M. A new paradigm of fatigue variability behavior and implications for life prediction. Materials Science and Engineering A 2007; 468-470: 23-32.

[90]   Jha, S.K. and Larsen, J.M. Random heterogeneity scales and probabilistic description of the long-lifetime regime of fatigue. Fourth International Conference on Very High Cycle Fatigue (VHCF-4). J. E. Allison, J. W. Jones, J. M. Larsen and R. O. Ritchie. Ann Arbor, Michigan, USA, The Minerals, Metals & Materials Society (TMS) 2007; 385-396.

[91]   Wang, Q.Y., Bathias, C., Kawagoishi, N. and Chen, Q. Characterization of S-N curve in gigacycle fatigue. SPIE proceedings series, International conference on experimental mechanics N^o3, Beijing, China 15-17 October, 2001; 2002L 4537:213-216.

[92]   Furuya, Y., Abe, T. and Matsuoka, S. Inclusion-controlled fatigue properties of 1800 MPA-class spring steels. Metallurgical and Materials Transactions A: Physical Metallurgy and Materials Science 2004; 35 A(12):3737-3744.

[93]   Zhang, M., Zhang, J. and McDowell, D.L. Microstructure-based crystal plasticity modeling of cyclic deformation of Ti-6Al-4V. International Journal of Plasticity 2007; 23(8):1328-1348.

[94]   Kueppenbender, I. and Schuetze, M. Deformation behavior of NiO scales on Ni in argon and air at temperatures from 20 to 800°C with respect to the relief of growth stresses. Oxidation of Metals 1994; 42(1-2):109-144.

[95]   Bruns, C. and Schutze, M. Investigation of the Mechanical Properties of Oxide Scales on Nickel and TiAl. Oxidation of Metals 2001; 55(1-2):35-68.

[96]   Johnson, J.B., Nicholls, J.R., Hurst, R.C. and Hancock, P. (1978). The mechanical properties of surface oxides on nickel-base superalloys. I. Oxidation. Corrosion Science 1978 18(6):527-541.

[97]   de Bussac, A. Prediction of the competition between surface and internal fatigue crack initiation in PM alloys. Fatigue and Fracture of Engineering Materials and Structures 1994; 17(11):1319-1325.

[98]   Lemaitre, J. and Chaboche, J.L. Mechanics of Solid Materials. Cambridge University Press, 1990.
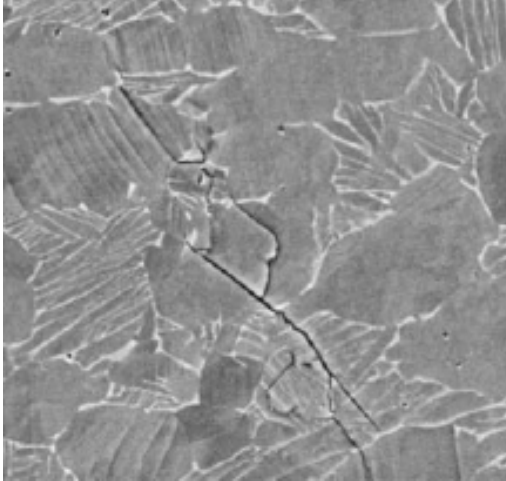
Crack formation due to intense shear along the slip band of Ti-6Al-4V [25].
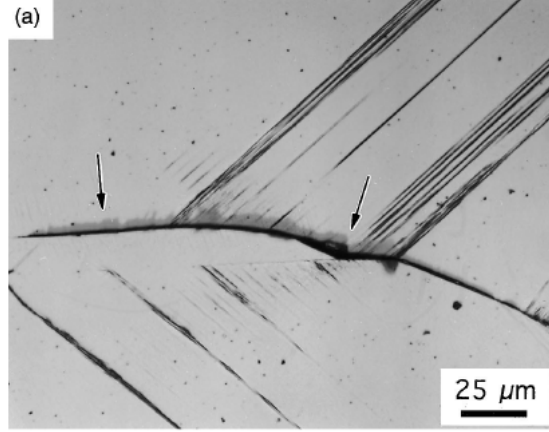
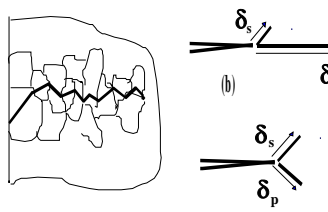Slip band impingement on grain boundary of polycrystalline nickel [26].

Intensive shear along slip band

$$\gamma_{net}^{p*}\left(1+K_z^{'}\frac{\sigma_{GB}^{n*}}{\sigma_y}\right)$$

Slip band impingement

$$\frac{\Delta\gamma_{max}^{p*}}{2}\left(1+K^{'}\frac{\sigma_{max}^{n*}}{\sigma_y}\right)$$
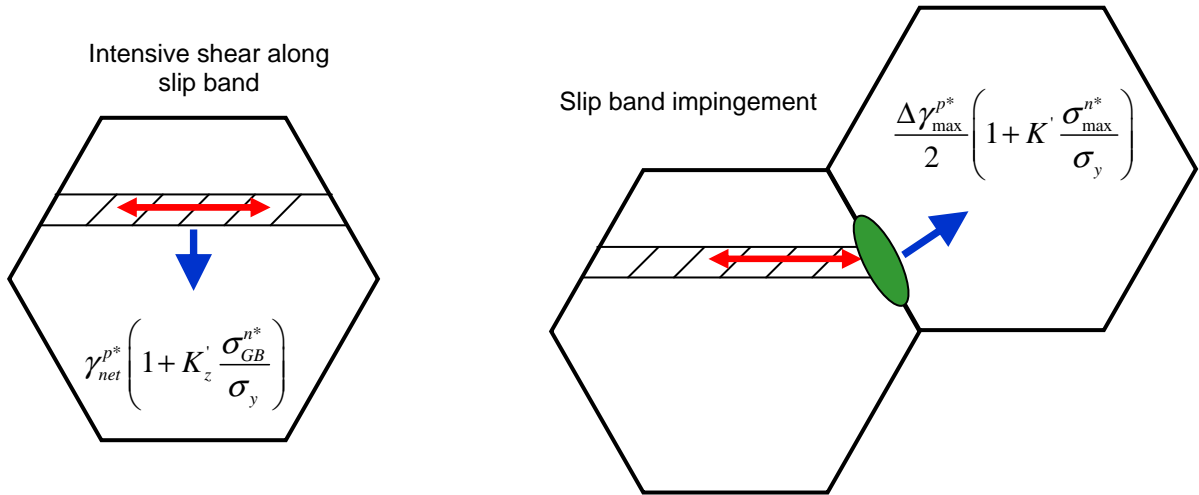
Figure 1.   Candidate fatigue indicator parameters (FIPs) with combined effects of plastic shear strain and normal stress on critical planes for crack nucleation and early growth along slip bands or grain boundaries for polycrystalline Ti-6Al and Ni.

$$\left(\frac{da}{dN}\right)_{MSC/PSC} = G\left(\Delta CTD - \Delta CTD_{th}\right)$$

Microstructure-sensitive driving force

$$CTD = \sqrt{CTOD^2 + CTSD^2}$$

$$\left(\frac{da}{dN}\right)_{LC} = F\left(\Delta K_{eff}^{\ M} - \Delta K_{th}^{\ M}\right)$$

or

$$\left(\frac{da}{dN}\right)_{LC} = U\left(\Delta K, K_{max}\right) - H\left(\Delta K_{th}\right)$$

$$\frac{da}{dN} = \max\left[\left(\frac{da}{dN}\right)_{MSC/PSC}, \left(\frac{da}{dN}\right)_{LC}\right]$$

Figure 2. Crack growth rates for MSC/PSC and LC components of total fatigue life, with the former dominant in the HCF and VHCF regimes. Inset figure shows Stage I to Stage II transition and relation of ΔCTD to primary and secondary slip slip at the crack tip for MSC regime [27].
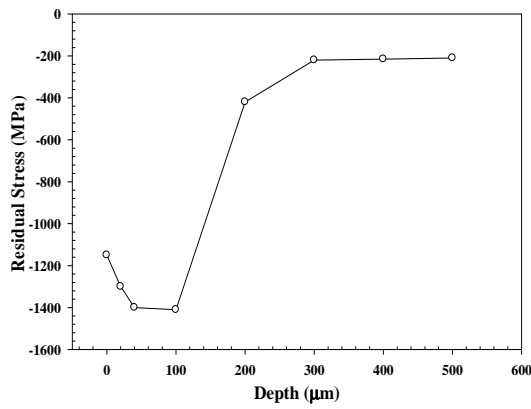
(a)
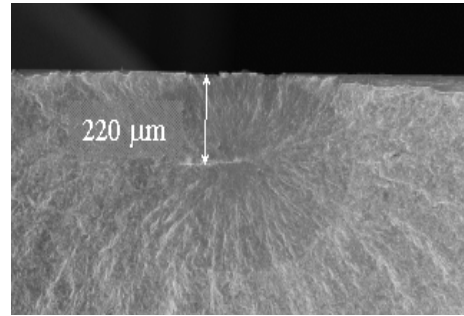
(b)

Tooth Fracture Surface   Mating Fracture Surface
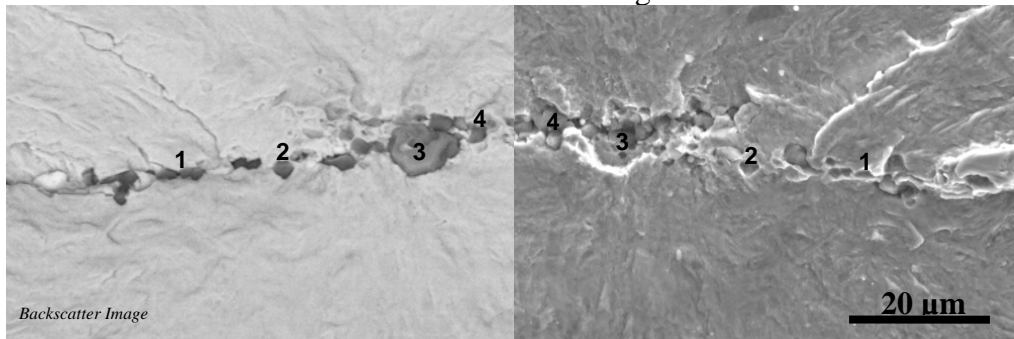
(c)

Figure 3. (a) Variation of residual stress after shot peening with depth, (b) SEM micrograph of fracture surface indicating the depth of fatigue crack origin, and (c) Backscatter SEM image of crack initiation zone showing characteristic inclusion sizes, cluster and debonding of inclusion-matrix interfaces [44].
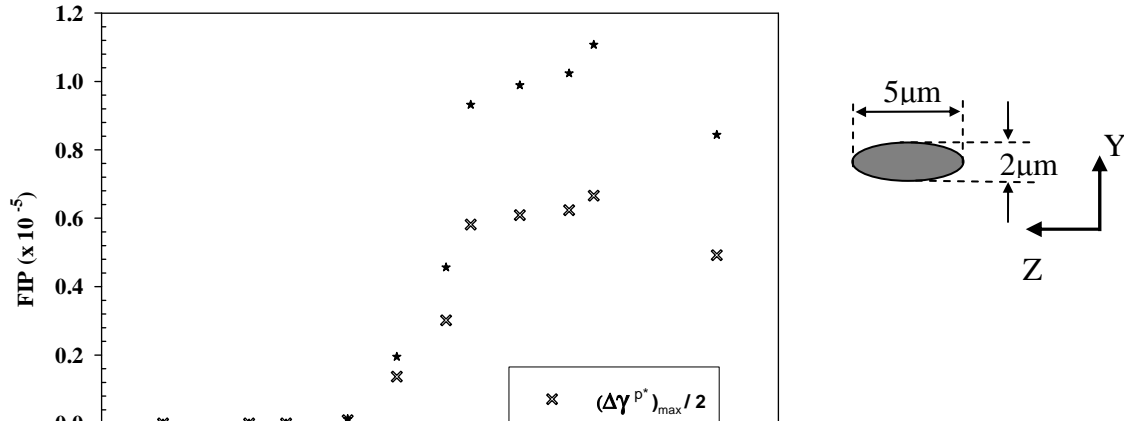
Figure 4. Variation of nonlocal maximum cyclic plastic shear strain amplitude and FS parameter with depth for single cracked particle.
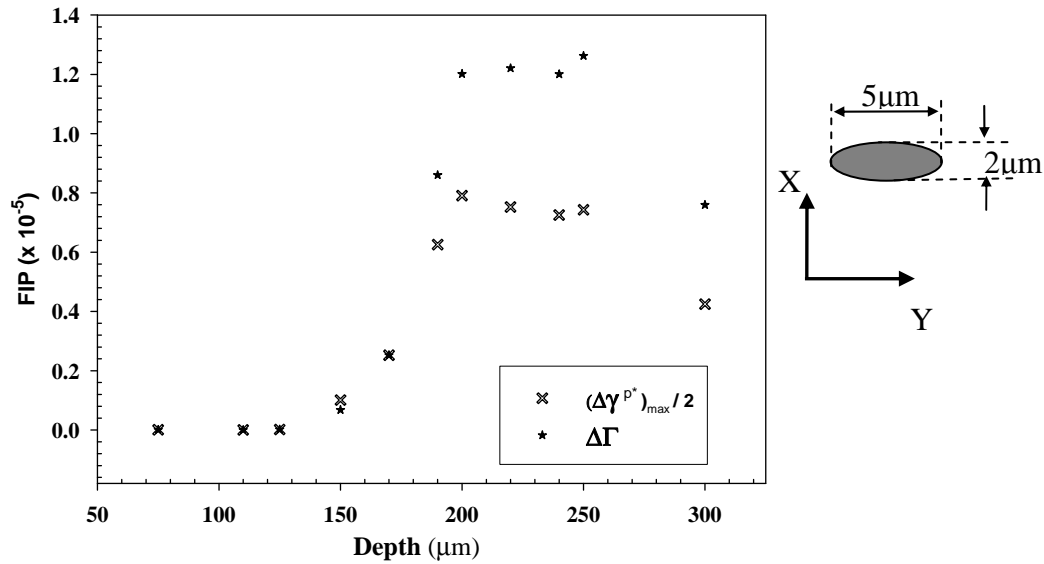
Figure 5. Variation of nonlocal maximum cyclic plastic shear strain amplitude and FS parameter with depth for single partially debonded particle.
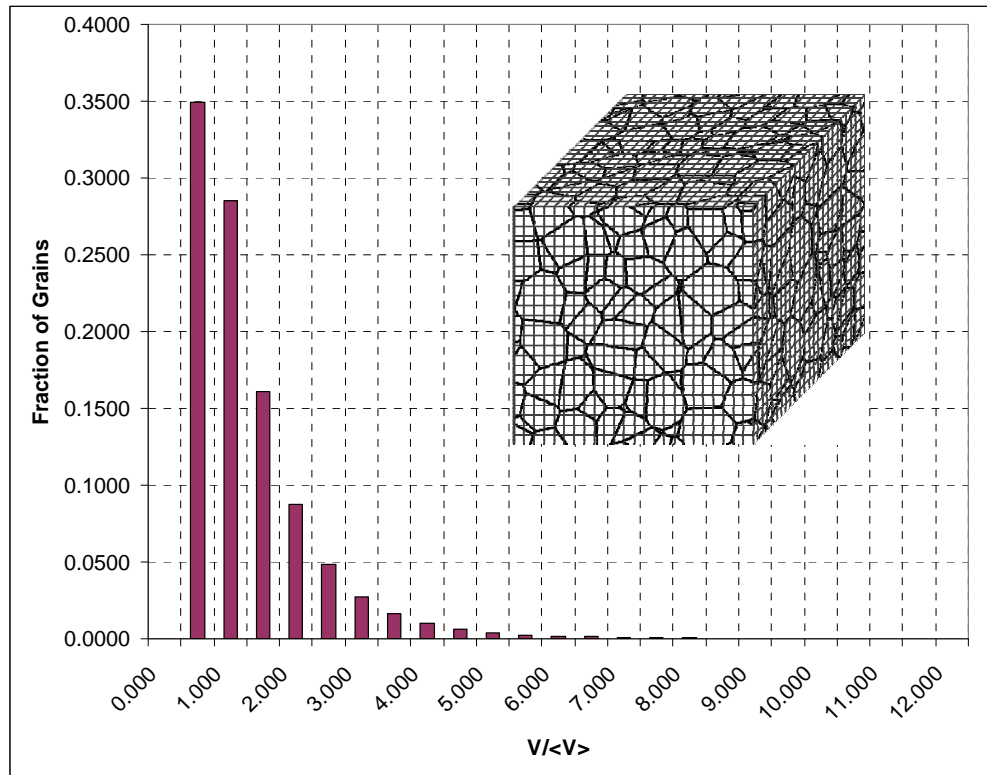
Figure 6. Log normal distribution of grain volume V normalized by imposed average grain volume $<V>$ of 1×10^{-5} mm^3 which corresponds to a cube root grain size of 20 μm.
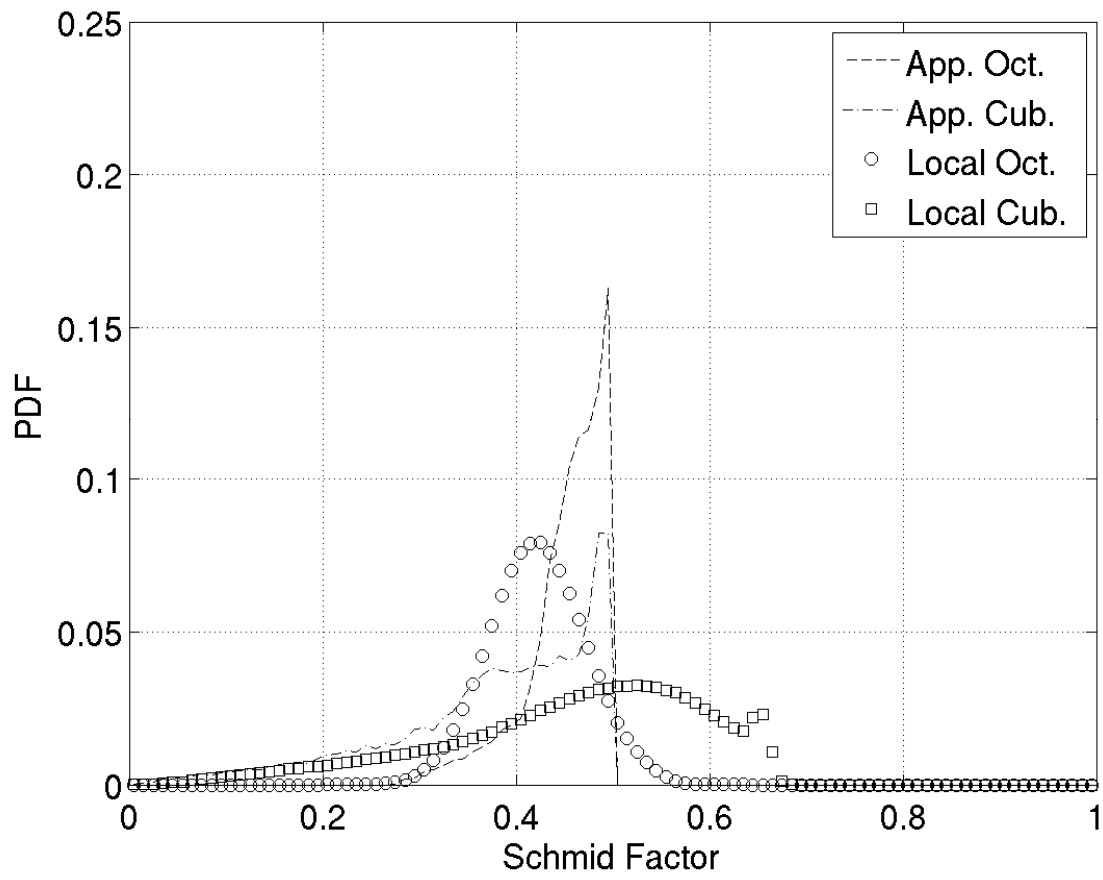
Figure 7. Probability density of the apparent and local Schmid factors over all 100 microstructure instantiations.
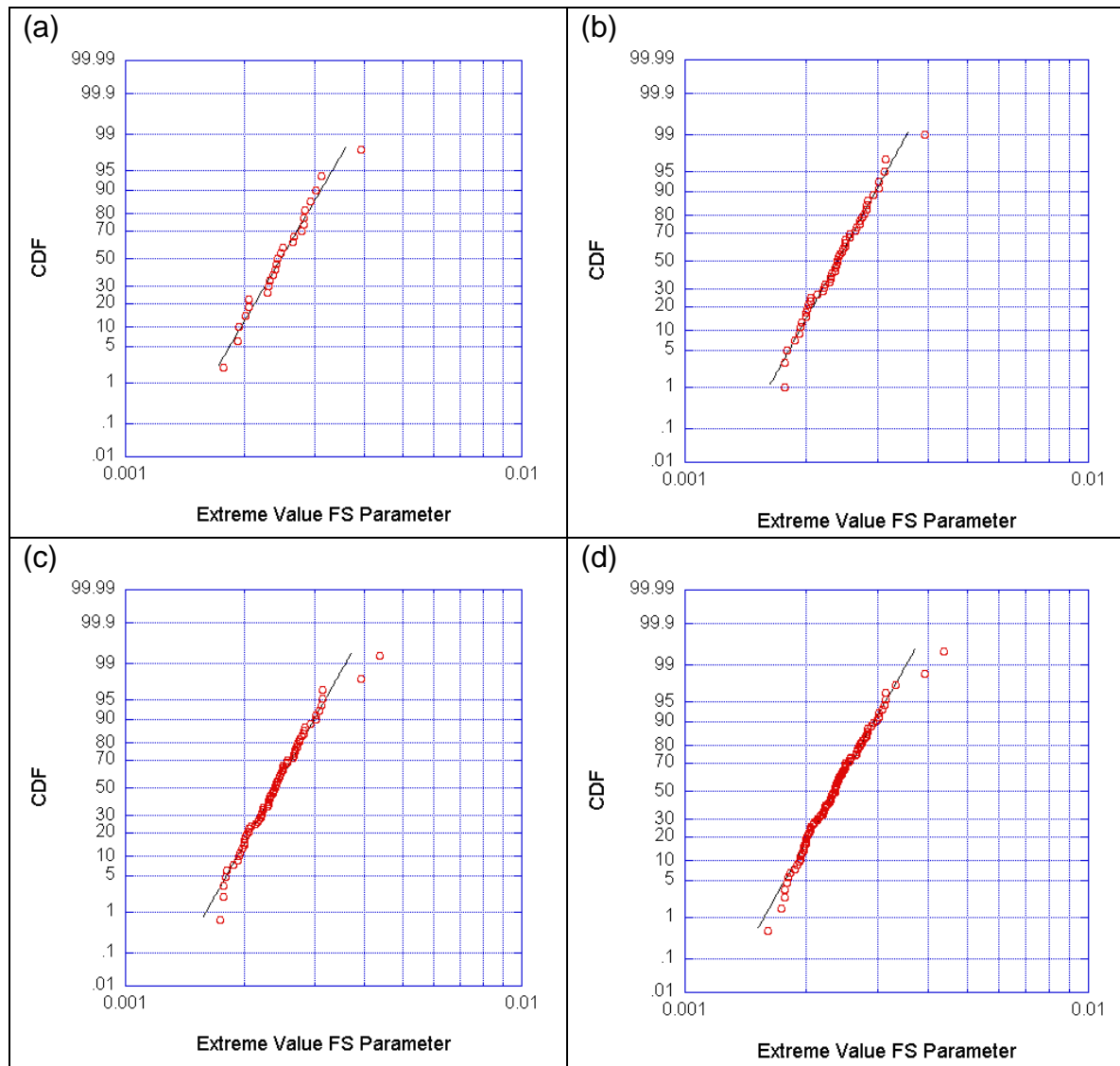
Figure 8. Cumulative distribution functions for extreme value Fatemi-Socie FIP for sample sizes of (a) 25, (b) 50, (c) 75 and (d) 100 simulated SVEs. In each case the exponential fit is given as a solid black line.
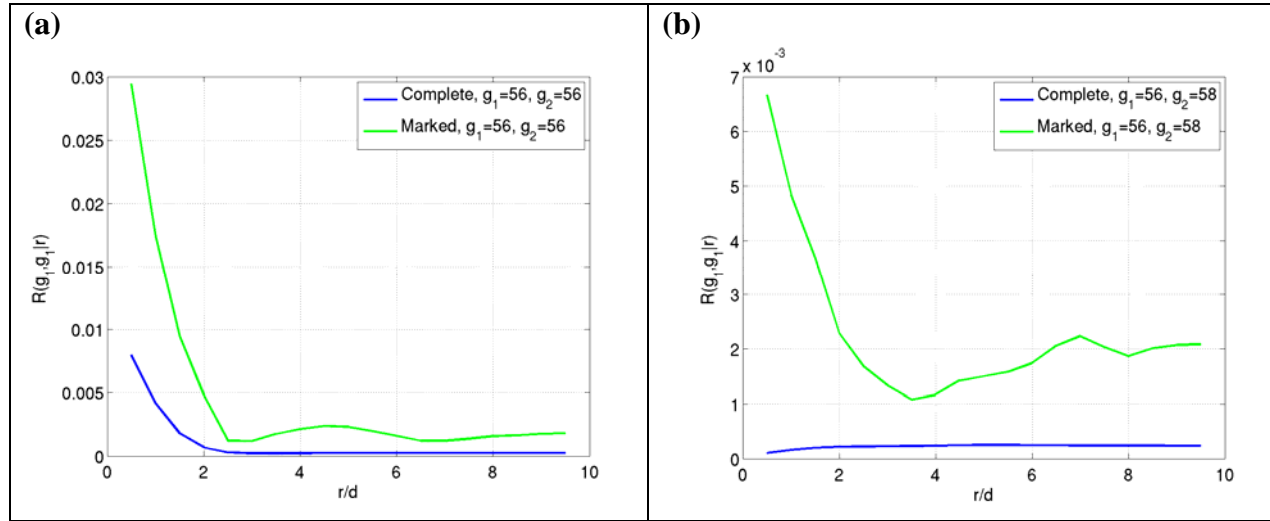
Figure 9. For IN 100 the (a) complete radial and extreme value marked radial distribution of orientations $g_1 = 56$ and $g_2 = 56$ and (b) complete radial and extreme value marked radial distribution of orientations $g_1 = 56$ and $g_2 = 58$ are plotted. The distance r that separates the two orientations is normalized against the average grain size d. Here, g_1 and g_2 describe the particular orientation and represent β and β', respectively.
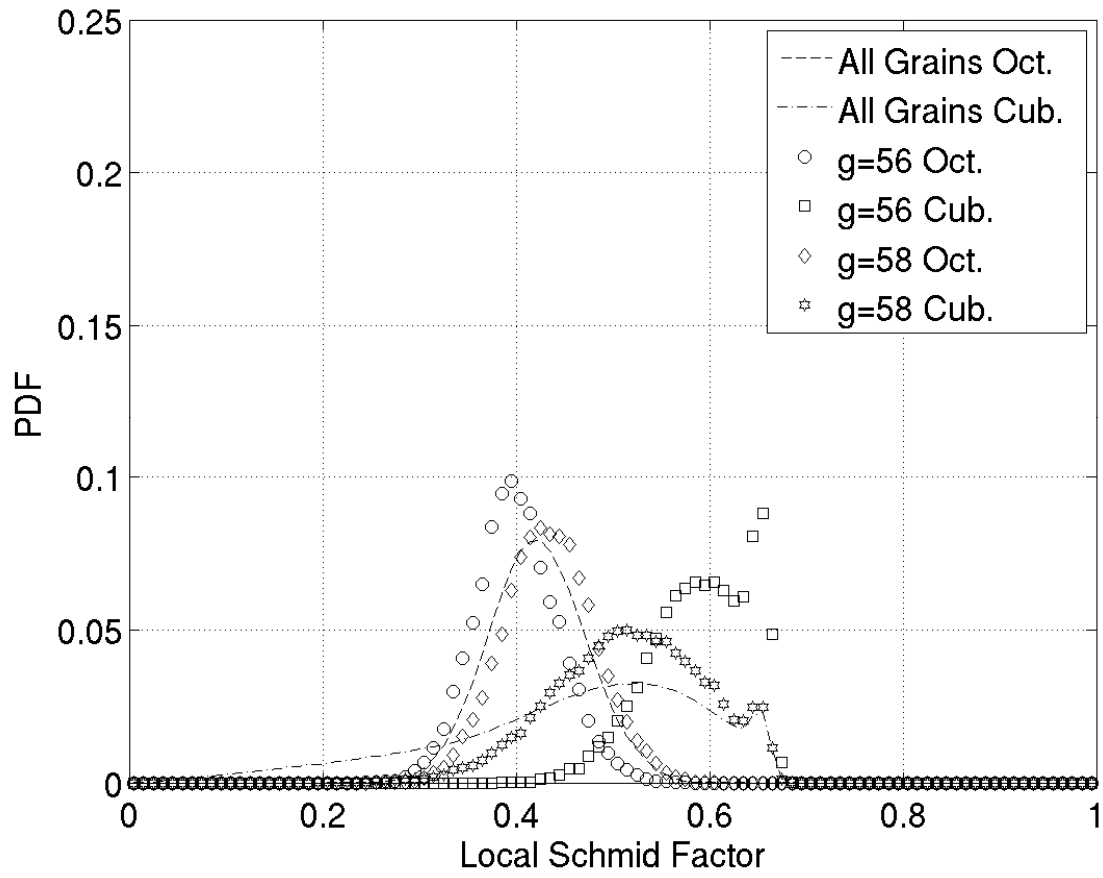
Figure 10. Probability density of the local Schmid factor for the complete set of all grains and for grains with orientation g = 56 and orientation g = 58.
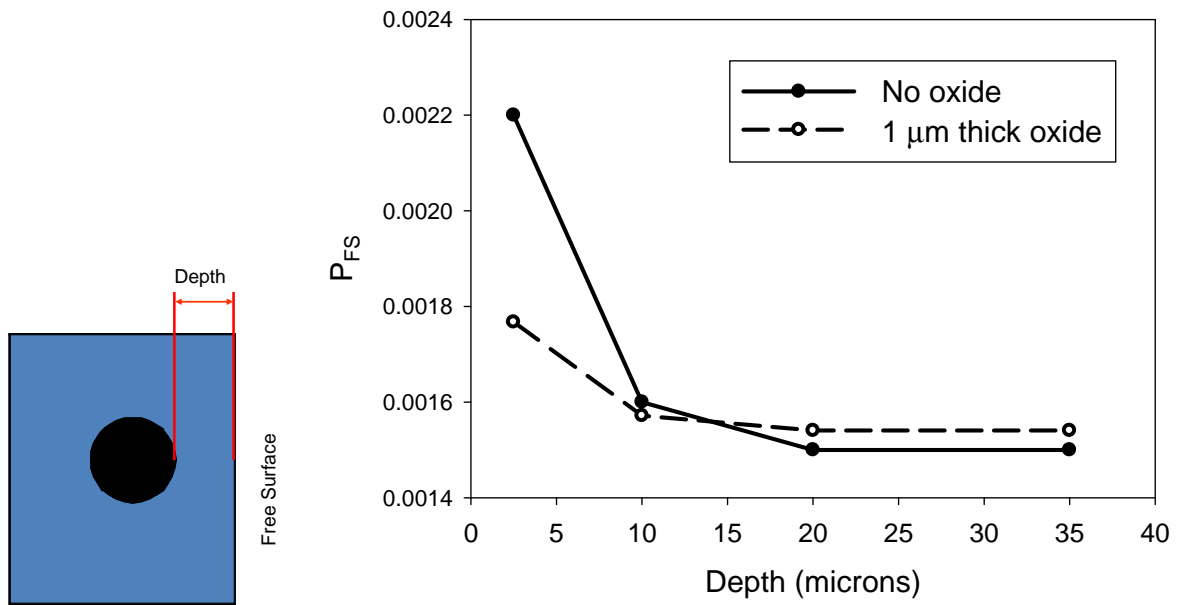
Figure 11. Nonlocal Fatemi-Socie parameter (P_{FS}) as a function of inclusion depth from free surface (symbols are computed datapoints). Uniaxial cyclic tension-tension stress (R = 0) is applied in the vertical direction, parallel to the free surface.
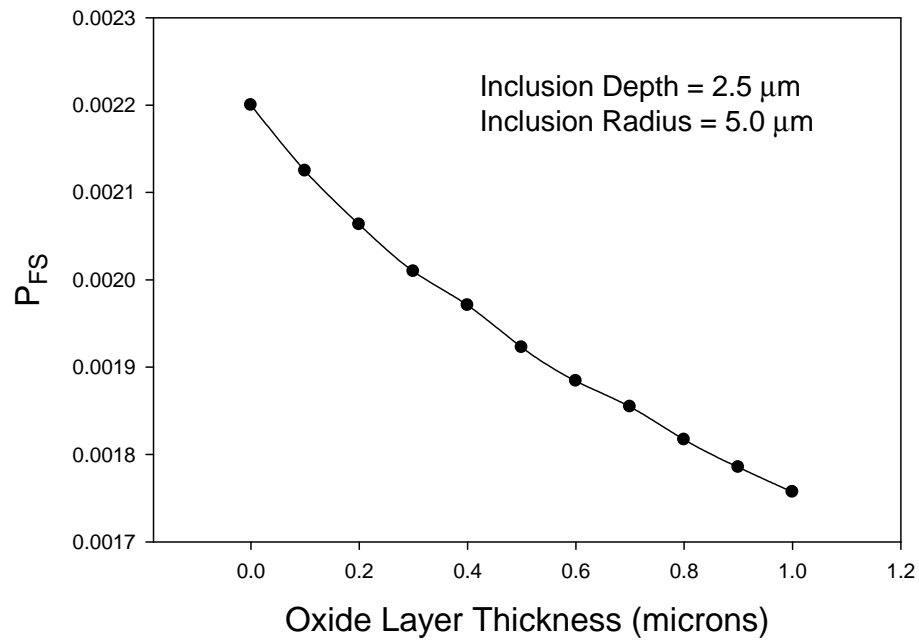

Figure 12. FS parameter versus oxide layer thickness (symbols are computed datapoints).
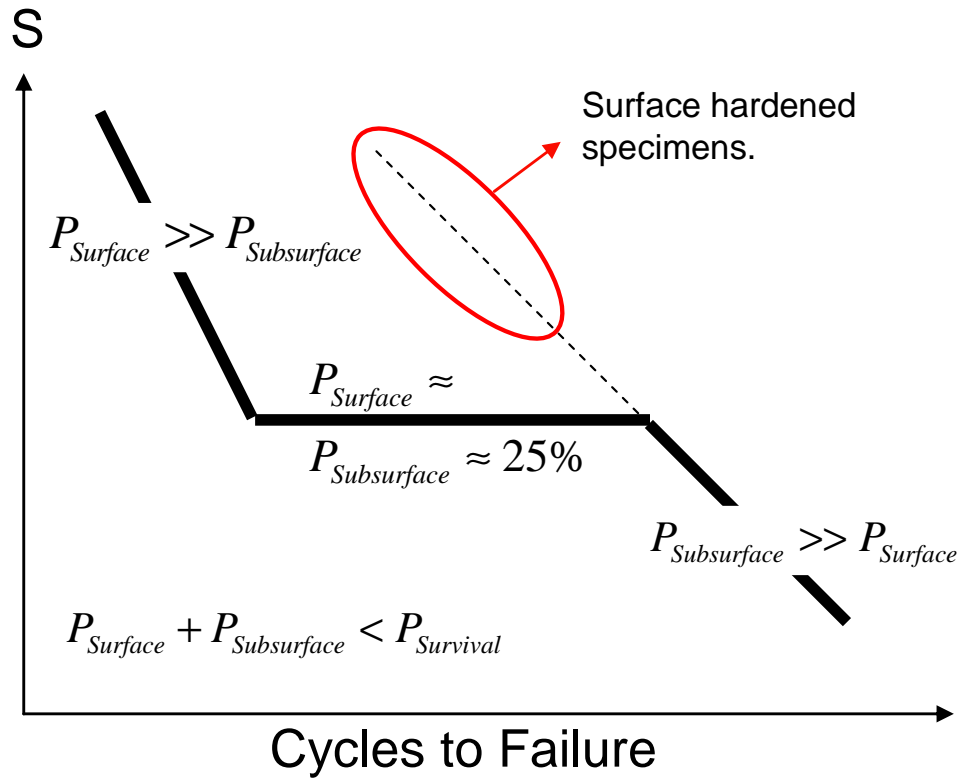
Figure 13. Probabilities of surface and subsurface fatigue crack initiation for HCF to VHCF transition.

Table 1. Composition of C61 steel (wt %).

Alloy	Co	Cr	Ni	Mo	V	C	Fe
C61	18.0	3.5	9.5	1.1	0.08	0.16	Bal.

Table 2. Material parameters for martensitic steel.at room temperature.

Material	E (GPa)	ν	Yield Strength (MPa)	Kinematic Hardening Parameters (c, r)
Matrix	194	0.28	970	112,000, 200
Inclusion	400	0.20	N/A	N/A
Surface Layer	194	0.28	N/A	N/A